MASTERARBEIT / MASTER THESIS

Titel der Masterarbeit / Title of the Master Thesis

"Setup and operation of an optical frequency comb resolved Fourier-transform infrared spectrometer"

verfasst von / submitted by

Maximilian Prinz, BSc

angestrebter akademischer Grad / in partial fulfilment of the requirements for the degree of

Master of Science (MSc)

Wien, 2022 / Vienna, 2022

Studienkennzahl lt. Studienblatt / degree programme code as it appears on the student record sheet:	UA 066 876
Studienrichtung lt. Studienblatt / degree programme as it appears on the student record sheet:	Masterstudium Physik
Betreut von / Supervisor:	Ass.-Prof. Dipl.-Phys. Dr. Oliver H. Heckl
Mitbetreut von / Co-Supervisor:	

Abstract

This thesis describes the construction and operation of a variable, high-resolution (0.0025 cm^{-1}, 75 MHz) Fourier transform spectrometer. This entails both the assembly of the optical setup, as well as the implementation of an acquisition and processing software (in combination with a graphical user interface) in the Python programming language. The developed software makes use of an instrumental-lineshape-correction algorithm, which allows to surpass the nominal resolution of the instrument when combined with an optical frequency comb.

The performance of the instrument was thoroughly tested by measuring the modulation efficiency, and the signal-to-noise ratio calculated from measured 100% lines.

Proper operation of the evaluation software was tested by comparing results for previously-recorded interferograms of a cavity-filtered, stabilized optical frequency comb with repetition rate of 251 MHz and carrier envelope offset of 16.7 MHz, with those of another research group. We were thus able to demonstrated the reliability of the employed algorithm, achieving sub-nominal resolution on the order of the linewidth of individual comb modes.

In order to keep the measurement time at a minimum, the execution of the developed software was optimized using a multi-threaded approach. Key parameters like thread-execution time and duty cycle efficiency, were benchmarked accordingly.

Zusammenfassung

Diese Arbeit beschreibt den Aufbau und die Funktionsweise eines variablen, hochauflösenden (0,0025 cm^{-1}, 75 MHz) Fourier Transformations-Spektrometers. Dies umfasst sowohl den Aufbau des optischen Apparates, als auch die Implementierung einer Erfassungs- und Verarbeitungssoftware in Kombination mit einer grafischen Benutzeroberfläche in der Programmiersprache Python. Die entwickelte Software nutzt einen Instrumental-Lineshape-Korrekturalgorithmus, welcher es ermöglicht die nominelle Auflösung des Instruments, in Kombination mit einem optischen Frequenzkamm, zu übertreffen. Die Leistung des Instruments wurde getestet, indem die Modulationseffizienz gemessen wurde, und das Signal-Rausch-Verhältnis aus gemessenen 100%-Linien berechnet wurde.

Die ordnungsgemäße Funktion der Auswertesoftware wurde getestet, indem Ergebnisse für zuvor aufgezeichnete Interferogramme eines cavity-gefilterten, stabilisierten optischen Frequenzkamms mit einer Repetitionsrate von 251 MHz und einem Offset von 16,7 MHz mit denen einer anderen Forschungsgruppe verglichen wurden. Wir konnten somit die Zuverlässigkeit des verwendeten Algorithmus demonstrieren und eine subnominale Auflösung in der Größenordnung der Linienbreite einzelner Kammmoden erreichen.

Um die Messzeit möglichst gering zu halten, wurde die Ausführung der entwickelten Software durch einen Multithreading-Ansatz optimiert. Schlüsselparameter wie Thread-Ausführungszeit und Arbeitszykluseffizienz wurden entsprechend bewertet.

Acknowledgements

First of all I want to thank my supervisor Ass.-Prof. Dipl.-Phys. Dr. Oliver H. Heckl for the opportunity to join his team and work on an amazing and resourceful subject. Thank you for the trust you set in me and I look forward to hopefully many fruitful years of work with you.

Special thanks go out to PhD candidate Mag. Lukas W. Perner, BSc for his huge amount of patience in coaching and teaching me, on occasion having to explain the same subject to me multiple times. The example you set for work ethics and methodology made me a better scientist and also showed me the benefit, of having a good laugh in the office once in a while.

I want to extent my thanks to all the team members, past and present, who welcomed me with open arms and supported me along the past year and hopefully in the coming years as well. Thank you Georg Winkler, Jakob Fellinger, Valentina Shumakova, Vito Fabian Pecile, Collin Aldia Pulickal Edwin, Dido Denier van der Gon, Michael Leskowschek and Jonas Ballentin.

I sincerely want to thank Prof. Piotr Masłowski, PhD and Dominik Charczun, Msc of the Niclaus Copernicus University in Toruń for providing the necessary OFC data for this project as well as being available for any questions during the process of debugging the core algorithm for sub-nominal resolution.

Regarding my fellow students at the Institute of Astrophysics and the Faculty of Physics of the University of Vienna, I feel like a lot of our university life was a collaborative effort. I would not have wanted to miss a second of it. Special thanks go out to my dear friend Michael Leskowschek, who shared my journey from the first day I stepped into the Faculty of Physics. Thank you and Sarah for keeping me company and thank you for the countless hours, days and weekends we spent together. Furthermore I want to thank my various friends outside of academia, Belinda Pachoinig, Kristina Loike, Viktoria Bittner and all the others who had to put up with me talking enthusiastically about my work.

Considering my family members, I want to thank each and one of them for their support, especially my mum Claudia Strametz and my dad Gerhard Prinz as well as my brother Raphael Benjamin Prinz. Thanks for your understanding and care, even when things got rough I always knew I could count on you.

Contents

1. Introduction

1.1. State of Research

Fourier transform spectrometers are a widely-used and well-established tool in modern science, with applications in a vast range of disciplines, including medicine [1, pp. 244-247], environmental science [2], the study of electronic properties of materials [3, pp. 237-248], as well as optical properties of materials, like the refractive index [4]. Also, the recently-launched and now-operational James Webb Space Telescope (JWST), uses infrared spectroscopy to generate new insights in astronomy [5], [6]. However, as ground-breaking as direct observations of the JWST are considered to be , such astronomic measurements rely on comparison with precision reference spectra recorded in controlled laboratory environments on Earth, like those provided by the HITRAN database [7]. Such experiments serve to provide databases like HITRAN with the necessary high-resolution absorption-line lists, also enabling numerical simulations and spectral decomposition.

With the advent of femtosecond mode-locked lasers in Fourier transform spectroscopy [8], [9], [10] in the mid to late 2000s, a new era of light sources began to take form. Such mode-locked lasers combine a broad spectral range with excellent spatial and temporal coherence properties, making them optimal sources for high resolution spectroscopy.
While employing frequency-stabilized mode-locked lasers, so-called optical frequency combs, improved many sub-fields of spectroscopy, like Ramsey-comb spectroscopy or direct frequency comb spectroscopy [11], it also allowed for the development of experimental and numerical methods to overcome the size-limited resolution of Michelson-based Fourier transform spectrometers [12], [13], causing a paradigm-shift in high-resolution optical frequency comb spectroscopy. The performance of this method was demonstrated only recently, when line positions of older HITRAN2016 data for bands of $^{14}N_2{}^{16}O$ at 7.8 μm were improved by one order of magnitude [14]. Other applications of the ILS-free method include the precise measurement of cavity loss and dispersion as demonstrated by [15]. This drastic increase in resolution, together with steady advancements in optical components, such as high-reflectivity crystalline mirrors [16], will enable novel approaches to high-precision spectroscopy, among them the measurement of Doppler-broadening-free transitions via comb-mode resolved Lamb-dip spectroscopy.

1.2. Aims of the Thesis

As Fourier transform spectrometers have a long tradition, dating back to the 19th-century [17], these instruments are itself tried-and-tested tools for many applications. In order to improve on such a well-established measurement scheme, creative workarounds for inherently-limiting properties, such as the instrument-size-dependent resolution, are needed. At the same time, cost-efficiency and instrument size are important factors in the entire innovation process.

This thesis aims to provide a concise description of the operation principles of a Fourier transform spectrometer, while also emphasizing the advantages of using an optical frequency comb instead of a conventional incandescent source for absorption measurements. Furthermore, a detailed report on the construction and performance of an optical frequency comb Fourier transform spectrometer will be given.

This apparatus, built in-house with commercially available components, has a maximum resolution of 0.0025 cm^{-1}. Furthermore, the data acquisition, resampling and processing software was written and optimized alongside the design and building process of the spectrometer. This software allows recording and processing of interferograms to obtain instrumental-lineshape-free spectra, given that a stabilized frequency comb is used as source. In the entirety of the development process, we focused on a fast and easily adaptable code without the need of proprietary software. The measurement setup aims to deliver high-resolution spectra in as little time as possible, as future efforts will require the recording of many such spectra to obtain optimal signal-to-noise and resolution. A GHz-linewidth reference laser and an in-house-built near-infrared mode-locked laser were available to obtain performance measurements on the apparatus.

Furthermore, we demonstrate that the system is ready for measurements with sub-nominal resolution when combined with an optical frequency comb, further highlighting the benefits of such light sources. The results of our approach are projected to be on par with established and published implementations, while drastically improving computational efficiency. Especially for high-precision spectroscopy, this improvement in computation time will allow for an increase in resolution of several orders of magnitude by recording and processing many individual spectra and subsequently combining them to achieve much higher resolutions in the final result.

The here-presented measurement setup was planned for best performance in the 3–5 µm mid-infrared region, but the approach is inherently broadband and only limited towards lower wavelengths by the bandwidth limitations of current oscilloscopes and analog-to-digital converters.

2. Basics and Theory

In order to understand the process leading to spectra with sub-nominal resolution, first the underlying principles of a Fourier transform spectrometer (FTS) are discussed in 2.1.1, stretching from monochromatic to continuous sources. The effects resulting from the finite size of these instruments, as well as problems that can arise during operation, are discussed in 2.2. The implementation of optical frequency combs (OFCs) instead of conventional broadband sources mitigates some of these problems as described in 2.3.

Inherent performance issues of a FTS together with external and internal sources of noise are however still problematic. Thus a number of noise sources are presented in 2.4, as well as a set of performance tests aiming to identify any underlying issues.

In order to correctly set up the spectrometer, the basics of digital signal processing are covered in 2.5. A concise overview of the properties of the continuous Fourier transform as well as the discrete complex Fourier transform and the fast Fourier transform are given in 2.6. These properties serve as the tools which are employed in 2.7, where the engineering of the FTS sampling scale leads to the desired sub-nominal resolution, using the precise information of the OFC in order to match the zero crossings of the instrumental line shape to the exact comb mode positions.

2.1. Michelson-based Fourier Transform Spectrometers

Michelson interferometers are a well established tool across various scientific fields, especially in Fourier transform infrared (FTIR) spectroscopy [18]. Although many variations exist, their underlying principle remains the same: By splitting an incoming beam of light into two arms, introducing a variable optical path difference to them and letting them recombine, an interferogram is created by constructive and destructive interference of the two beams. Such an interferogram contains the complete spectral information of its source, which can be recovered by the Fourier transform, generating its spectrum. Compared to grating based spectrometers, a FTS profits from three main advantages: Because an interferogram contains information about all wavelengths, spectra can be recorded n times faster than grating based instruments, where n gives the number of resolution elements of the spectrum [18]. This leads to an increase of the signal-to-noise ratio with factor $\sqrt{n}$, which is called the multiplex advantage. Second, the throughput advantage stems from the fact, that no intensity loss occurs in a FTS due to gratings and slits [18]. Third, the advantage in wavenumber precision is achieved by propagating a stable reference laser parallel to the unknown signal and using it to calibrate the spectra.

To give a more detailed view on these basic concepts, the theory and operation of a Michelson interferometer is discussed in 2.1.1, restricting itself on the use of rapid-scan interferometers, excluding step-scan interferometers entirely. Any interested reader is referred to [19] for a detailed explanation of the latter.

2.1.1. Theoretical Background with Monochromatic Light Sources

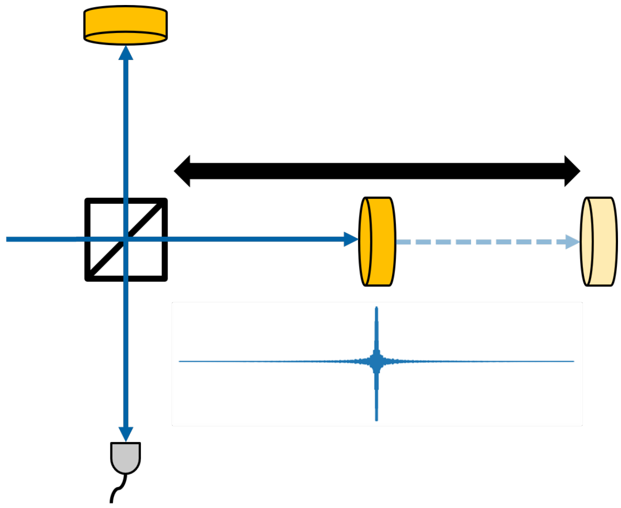

Figure 2.1.: Schematic drawing of a Michelson interferometer. Light entering on the left is split using a beamsplitter and travels to a fixed mirror (top) and a movable mirror (right). Depending on the position of the latter, a difference in optical path length between the beams is introduced, leading to an interferogram as depicted below the variable interferometer arm. For zero path difference the interferogram of a broadband source will show a maximum. The variation in intensity of the interferogram during the scan is recorded via a photodiode (bottom).

The classical Michelson interferometer [17] as depicted in figure 2.1 consists of a beamsplitter and two planar mirrors, one of which is moving with a constant velocity in parallel to the direction to the incoming beam of light. The mirrors are set up perpendicular to each other, so that a beam of light that enters the beamsplitter gets separated into two arms which are both reflected at the corresponding mirror. At a certain point in time t, the light travelling along the scanning interferometer arm experiences an optical path difference (OPD) with respect to the fixed arm, also called retardation δ,

$$\delta = 2V_{\mathrm{m}}t \qquad (\mathrm{cm}) \tag{2.1}$$

which is a linear function of the mirror velocity V_{m}. The intensity of the recombined beam at the detector changes according to the position of the movable mirror, as the corresponding beam experiences a phase shift with respect to the non-moving interferometer arm. The position where the phase shift is zero, i.e. where the distance from the mirrors to the beamsplitter are equal, is called point of zero path difference (ZPD). In order to better understand the underlying principles a perfect monochromatic source can be taken into consideration. Such a light-wave, usually in FTIR described by its wavenumber (subscript 0 to emphasise monochromaticity)

$$\tilde{\nu}_0 = \frac{1}{\lambda_0(\mathrm{cm})} \qquad (\mathrm{cm}^{-1}), \tag{2.2}$$

will experience a π-phase shift, if the moving mirror is displaced by $\lambda_0/4$ resulting in a OPD of $\lambda_0/2$, depicted in figure 2.2 b). As the fixed and variable beam are out of phase they will interfere destructively and the intensity at the detector will be zero. By moving the variable mirror again for $\lambda_0/4$, the OPD becomes λ_0, resulting in a phase shift of 2π like figure 2.2 d). The beams are thus in phase again and interfere constructively, as will be the case for all retardations equal to an integer number of wavelengths λ_0 [19, pp. 20-22]. Assuming the variable mirror moves with constant speed V_m, the intensity at the detector will correspond to a sine wave, with maximum at ZPD, and consequently at OPD steps corresponding to λ_0. As the speed of the moving mirror controls how fast the OPD is scanned, the measured frequency of the beat note at the detector is down-converted from optical frequencies. One can thus interpret a FTS as a system, mapping optical frequencies to audio frequencies, while keeping their distribution fixed [20, p. 37].

The intensity at the detector is the sum of a constant DC component as well as a modulated AC component given by

$$I_\mathrm{det}(\delta) = 0.5 I(\tilde{\nu}_0)\Big(1 + \cos\left(2\pi\tilde{\nu}_0\delta\right)\Big), \tag{2.3}$$

with the source intensity $I\left(\tilde{\nu}_0\right)$, where only the modulated AC component contains spectral information [19, p. 20]. The idealized situation in equation 2.3 does not take into account that the measured intensity also depends on the sensitivity of the detector with regards to wavenumbers [19, p. 23]. Also the responses of the beamsplitter, used optics and amplifiers are unequal depending on wavenumbers. These factors remain constant for fixed wavenumber $\tilde{\nu}_0$ and together with the source intensity can be expressed as the single-beam spectral intensity $B\left(\tilde{\nu}_0\right)$

$$B(\tilde{\nu}_0) = 0.5 H(\tilde{\nu}_0) G(\tilde{\nu}_0) I(\tilde{\nu}_0) \tag{2.4}$$

This single-beam spectral intensity consists of the responsivity of the used optics $H\left(\tilde{\nu}_0\right)$ like the wavenumber dependent beamsplitter response, reflectivity of the used mirrors and the transmission response of focusing lenses. The response functions of electronic measurement devices are condensed into $G\left(\tilde{\nu}_0\right)$ and lastly the source intensity $I(\tilde{\nu}_0)$, together with any absorption features of interest [19, p. 23].

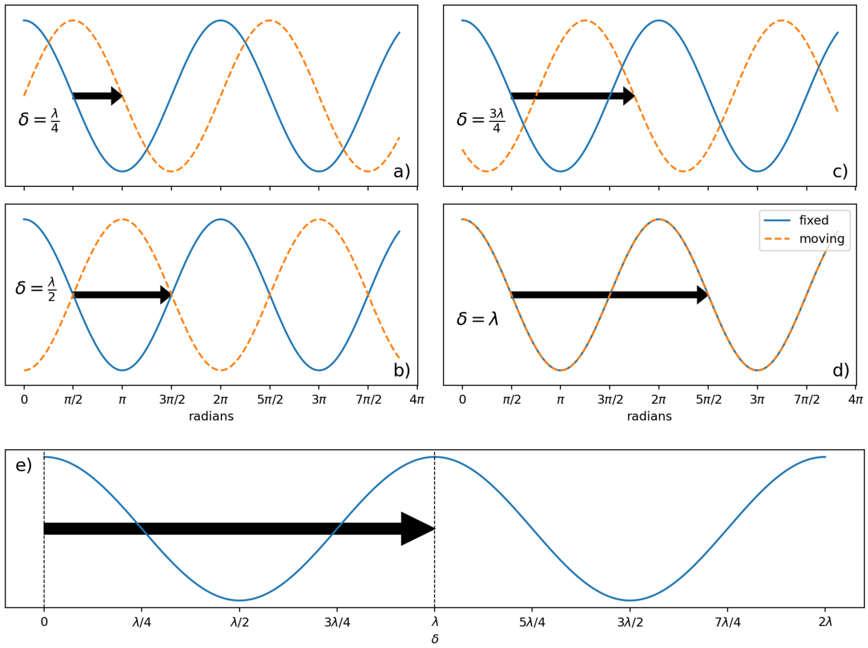

Figure 2.2.: Phase shift from fixed (solid blue) to moving (dashed orange) interferometer arm of a monochromatic wave at different retardations: a) OPD of one quarter-wavelength, b) OPD of one half-wavelength, c) OPD of one three-quarter-wavelength, d) OPD of one wavelength. e) Resulting interferogram as function of retardation δ. At ZPD, both waves interfere constructively until the retardation is equal to one half-wavelength where destructive interference occurs. If the path difference is increased further, the waves again interfere constructively for retardation of integer number of wavelengths. The black arrow indicates the range of δ covered in a)-d).

2.1.2. Theoretical Background with Polychromatic Light Sources

If n different monochromatic sources are measured, their individual cosine interferograms are summed as function of δ, resulting in an overall superposition of cosines $S\left(\delta\right)$

$$S(\delta) = \sum_{i=1}^{n} B(\tilde{\nu}_{\mathrm{i}})\Big(1 + \cos\left(2\pi\tilde{\nu}_{\mathrm{i}}\delta\right)\Big) \tag{2.5}$$

At every value of retardation, the phase shift as depicted in figure 2.2 will be different for every wavelength present in the source. While the set value of retardation induces constructive interference for one wavelength, it generates (completely) destructive interference for the others. The thus created OPD dependent interference pattern consists of a DC-offset from zero intensity, a modulating part and a decaying envelope function.

In practice, there are no monochromatic sources, even continuous wave lasers exhibit a non-negligible linewidth. As depicted in figure 2.2, the retardation for constructive interference has to be an integer multiple of the optical wavelength. Consequently, broadband sources with arbitrary frequencies will only be in phase at the point of ZPD, leading to a distinctive intensity maximum there, called the centerburst of the interferogram [19, p. 40]. An example is shown in figure 2.3, where Lorentzian emission lines were simulated and transformed to their corresponding interferograms with a direct cosine transform as given in equation 2.5. The interferogram in a) shows its intensity maximum at ZPD and is decaying for increased path difference. The envelope function of the interferogram is an exponential. The corresponding emission line in the spectrum is visible in b). The broader the width of the emission line, the faster does the envelope decay to zero. The interferogram as function of retardation of a spectral doublet is shown in c). The beat note is characteristic for two emission lines that are adjacent to one another in the spectrum, as depicted in d).

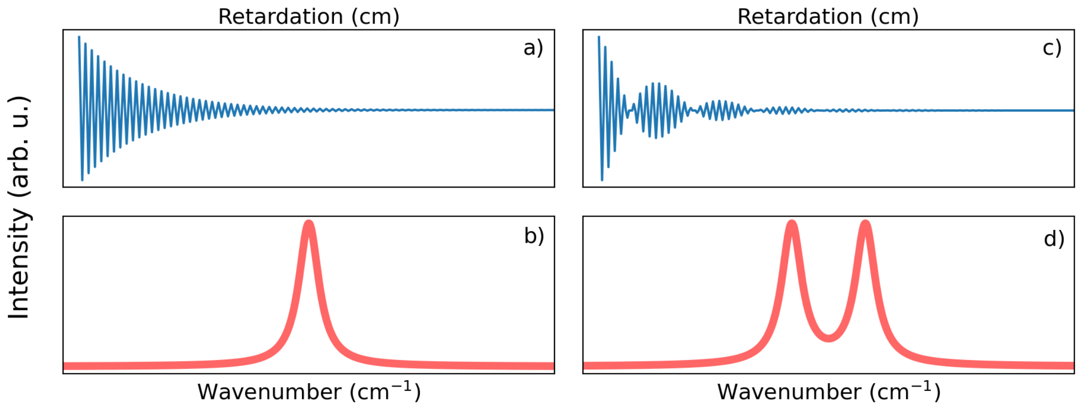

Figure 2.3.: Example of decaying envelope of an interferogram for sources with extended linewidth. a) Simulated interferogram with intensity maximum at zero retardation for single spectral profile. b) Emission line with Lorentzian profile calculated from the probability density function of a Cauchy distribution. c) Simulated interferogram of two monochromatic sources with extended linewidth. d) Emission lines spaced closely together resulting in characteristic beat note.

Especially continuous broadband light sources show a centerburst with a rapidly decaying envelope. The interferogram for continuous sources is given by the integral over all wavenumbers

$$S(\delta) = \int_{-\infty}^{+\infty} B(\tilde{\nu})\Big(1 + \cos(2\pi\tilde{\nu}\delta)\Big)\, d\tilde{\nu} \tag{2.6}$$

An important characteristic of $S(\delta)$ and the cosine is, that they are even and real functions. This means that $B(\tilde{\nu})$ must also be real and even [19, p. 26]. This single-beam spectral intensity is usually considered to be the spectrum of the corresponding interferogram. Consequently equation 2.6 can be rewritten to express this spectrum

$$B(\tilde{\nu}) = \int_{-\infty}^{+\infty} S(\delta)\Big(1 + \cos\left(2\pi\tilde{\nu}\delta\right)\Big) d\delta \tag{2.7}$$

as a function of the interferogram. As retardation δ and Intensity $S(\delta)$ can be expressed as a function of time following equation 2.1, the so-called Fourier frequency $f_{\tilde{\nu}}$ can be defined as

$$f_{\tilde{\nu}} = V_{\mathrm{o}}\tilde{\nu} \tag{2.8}$$

effectively returning the frequency of the interferogram corresponding to the spectral component $\tilde{\nu}$ of the frequency down-converted beat note on the detector. The optical velocity V_{o} gives the rate of change of retardation with time, being equal to two times the travel speed of the moving mirror $2V_{\mathrm{m}}$ for the Michelson interferometer in Fig. (2.1). For example, a typical Helium-Neon laser with wavenumber of 15797.79 cm^{-1} (474 THz), will be down-converted to 63.2 kHz for optical velocity of 4 cm/s. This linear relationship between measured frequency and optical wavenumber is severely limited by fluctuations of the constant mirror speed, prohibiting an easy calibration of the spectrum's abscissa.

Equations 2.6 and 2.7 correspond to the cosine Fourier transform (FT) pair and don't take the wavenumber dependent phase angle $\theta_{\tilde{\nu}}$ into account. Consequently, the complex Fourier transform pair gives the complete description of the relationship between interferogram and spectrum [19, p. 78]

$$S(\delta) = \int_{-\infty}^{+\infty} B(\tilde{\nu}) e^{2\pi i\tilde{\nu}\delta} d\tilde{\nu} \tag{2.9}$$

$$B'(\tilde{\nu}) = \int_{-\infty}^{+\infty} S(\delta) e^{-2\pi i\tilde{\nu}\delta} d\delta \tag{2.10}$$

where the resulting spectrum consists of a real part $\Re\{B'(\tilde{\nu})\}$ and an imaginary part $\Im\{B'(\tilde{\nu})\}$. The true real spectrum $B(\tilde{\nu})$ has to be calculated from the complex spectrum via phase correction as described in 2.6.5.

The above derivation allows for an intuitive link between the spectrum and the interferogram: The complete spectral information can in theory be recovered from an interferogram by a FT, if it could be measured over an infinitely long retardation δ. In practice such a measurement is impossible, so that the finite retardation will result in a finite spectral resolution. This and other real-world effects acting on an experimentally acquired interferogram and the derived spectrum are discussed in 2.2.

2.2. Effects acting on Interferometers

2.2.1. Resolution, Leakage and Constant-Space Sampling

A simple approach to obtain the relationship between the retardation and the resolution of a FTS is to imagine a spectral doublet $\tilde{\nu}_1$, $\tilde{\nu}_2$ of delta peaks with $\tilde{\nu}_1 < \tilde{\nu}_2$. For zero retardation, the two cosine waves corresponding to interferograms of the doublet are in phase and interfere constructively. Following equation 2.3, increasing the OPD between the interferometer arms results in the two waves going out of phase. After a retardation corresponding to the inverse of separation $\Delta\tilde{\nu} = \tilde{\nu}_2 - \tilde{\nu}_1$, the cosines are in phase again [18], [19, pp. 26-28]. To be in phase means that an integer multiple of periods n has been completed for the interferogram of $\tilde{\nu}_1$, and $(n+1)$ for the interferogram corresponding to $\tilde{\nu}_2$. The covered retardation Δ_{max} can be expressed as the number of cycles times the corresponding wavelength

$$\Delta_{\text{max}} = n\lambda_1 = (n+1)\,\lambda_2 \tag{2.11}$$

which in turn links the retardation (cm) with the nominal resolution (cm^{-1}) of a Michelson interferometer

$$\Delta\tilde{\nu} = \frac{1}{\lambda_2} - \frac{1}{\lambda_1} = \frac{(n+1)}{\Delta_{\text{max}}} - \frac{n}{\Delta_{\text{max}}} = \frac{1}{\Delta_{\text{max}}} \tag{2.12}$$

This is equal to the statement, that one full period of the beat note has to be measured, in order to resolve the responsible doublet. Industry standards like the Thorlabs Redstone OSA305 [21], or the Bruker Vertex 80v [22] are marketed to have maximal resolutions around 0.06 cm^{-1}, whereas big, high-end systems like the Bruker IFS 125HR can have resolution better than 0.0009 cm^{-1} [23].

The finite scan-length of a FTS can be viewed as a multiplication of the theoretically infinitely long signal with a boxcar function of length Δ_{max}. This restricts the signal to a symmetric interval around the center burst, called double-sided interferogram, or an interferogram covering only the retardation from zero to its maximum, called one-sided interferogram [19, p. 28]. The consequence of a multiplication of the interferogram with this boxcar function in the time domain, is a convolution of the single-beam spectral intensity with the instrumental line shape (ILS) function $f(\tilde{\nu})$ in the frequency domain [19, p. 28] (see 2.6) which is equal to

$$f(\tilde{\nu}) = 2\Delta\,\text{sinc}\,(2\pi\tilde{\nu}\Delta)\,, \qquad \text{for} \quad -\Delta \leq \delta \leq \Delta, \qquad \Delta = \Delta_{\text{max}}/2 \tag{2.13}$$

This function is displayed in figure 2.4, with its zero-crossings equally spaced by $(\Delta_{\text{max}})^{-1}$ wavenumbers. For a monochromatic source, the same function would be centered around the corresponding wavenumber. The above derivation of the spectral resolution links to the ILS, as the maximum of the sinc function of one wavenumber needs to be at the first

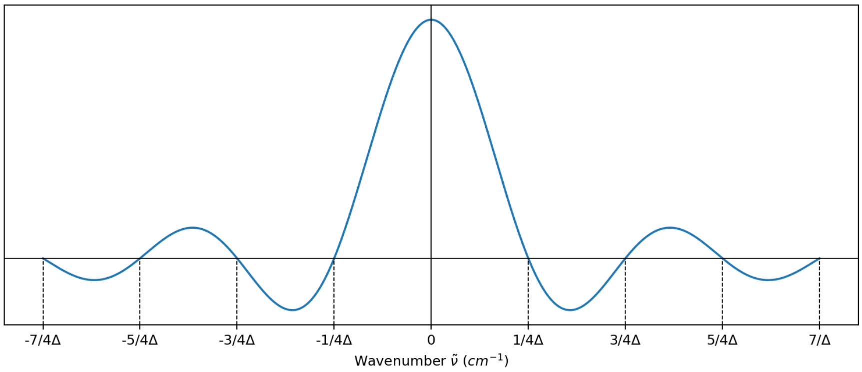

Figure 2.4.: ILS function $f(\tilde{\nu})$ which corresponds to the FT of a boxcar function from $-\Delta$ to Δ centimeters. The zero-crossings are spaced by $1/2\Delta = 1/\Delta_{\mathrm{max}}$ cm^{-1} and intersect the zero-level as indicated by the horizontal, solid black line. The abscissa's tick marks are used as visual aids and are plotted as dashed vertical lines.

minimum of the adjacent wavenumber in order to be resolved.

For two or more spectral samples follows, that the intensity at wavenumber $\tilde{\nu}$ carries contributions from all other wavenumbers in the spectrum. So-called apodization functions can be used to change the shape of the ILS and counteract the distinctive ringing [20, p. 93] in figure 2.4 and thus reduce the leakage of one sample to another. Such functions additionally prevent discontinuities at the edges of the sampled interferogram. After acquisition, the signal is multiplied by a symmetric window, leading to different ILS for different window functions. Every symmetric function around the center burst that decreases to zero over the desired range of retardation can be used as an apodization function, some common are the Norton-Beer, Hamming, triangular and Gaussian function. In general, using apodization functions decreases the spectral intensity and broadens the full width at half maximum (FWHM) of the center lobe compared to the side lobes [19, p. 33]. This means that an inherent trade-off is made when using an apodization function, the choice of which depending on the acceptable severity of the line broadening and intensity reduction.

The advantage in wavenumber precision, called Conne's advantage as described at the beginning of this chapter, relies on the correct sampling of the unknown signal with respect to a monochromatic reference laser that propagates alongside it. The interferogram of the monochromatic source as function of retardation is a cosine wave, its Fourier frequency given by the mirror velocity as given in equation 2.8. In order to sample the unknown signal correctly, usually the zero-crossings of the reference interferogram are determined and the signal interferogram gets interpolated precisely at those positions, as first demonstrated by [24]. This eliminates the problem of fluctuations in constant mirror speed, as the distance between two adjacent zero-crossings in terms of retardation, is always given by half the wavelength of the reference laser. The length of the interferogram is then truncated according to the desired resolution of the spectrum. If the interferogram is not sampled at constant intervals of retardation, every variation in mirror speed will result in a different Fourier frequency for fixed wavenumber $\tilde{\nu}$ and thus appear in the spectrum.

2.2.2. Divergence and Misalignment

Any extended source produces interference fringes that are imaged onto the detector plane due to the path difference in center and off-axis rays. The distance between two adjacent bright fringes is largest for zero retardation and decreases with longer retardation [19, p. 41]. If multiple fringes are recorded by the detector during a scan, the minima and maxima average to zero, and the modulation depth of the interferogram decreases. To prevent this loss in intensity modulation, only one fringe has to be measured, which corresponds to the central bright fringe at ZPD. To achieve this, an aperture is placed inside the beam path, called the Jacquinot stop. [19, p. 41-42].

The possible scan length of a FTS is in practice dependant on divergence of the light source that is being used. For a beam with divergence half-angle α (rad), the extreme and center rays will experience an additional path difference which leads to a loss in contrast in the detector, due to additional fringes, for increasing retardation. This results in a maximum accepted half-angle

$$\alpha_{\max} = \sqrt{\left(\frac{\Delta\tilde{\nu}}{\tilde{\nu}_{\max}}\right)} \tag{2.14}$$

for the interferometer [19, p. 44]. Incandescent broadband sources are in general poorly collimated and have high degrees of divergence, making the possible mirror travel range small. Lasers and OFCs as described in 2.3, are highly coherent with themselves and can be collimated easily over extremely long distances, basically eliminating the problem entirely. If the interferometer is misaligned, the image of the moving mirror will hit the detector at a different position than the image of the fixed mirror. The angle θ of misalignment decreases the spacing

$$d = \frac{\lambda}{\sin(\theta)} \tag{2.15}$$

of fringe maxima for a specific wavelength λ. This also leads to a reduction in fringe contrast, and consequently modulation depth of the interferogram. Lower wavelengths (higher wavenumbers) will show more fringes than higher wavelengths (lower wavenumbers). This results in the interferogram getting asymmetric, as the position of zero path difference changes depending on wavenumber [19, pp. 46-48]. Also the mirror tilt has to be kept lower than a threshold angle β during the scan, in order to keep the desired contrast for beam diameter D and highest occurring wavenumber $\tilde{\nu}_{\text{max}}$ [19, p. 49]:

$$\beta < \frac{1}{20D\tilde{\nu}_{\text{max}}} \tag{2.16}$$

The best way to eliminate the problem of mirror tilt, is to use cube-corner retroreflectors, made out of three planar mirrors mounted so that each mirror plane is perpendicular to the others, with the resulting output beam being parallel to the input beam [25].

2.2.3. Interference due to Etalons

An etalon is a linear optical cavity consisting of two planar surfaces separated by distance L [26, p. 192], as depicted in figure 2.5. A monochromatic light ray entering the optic gets refracted following Snell's law, and partly reflected on the first boundary layer. The transmitted ray hits the second boundary layer and is again partly transmitted and partly reflected. From this follows, that a non-zero part of the light ray oscillates inside the optical medium. As part of the beam is transmitted after one roundtrip in the cavity, the time delay between it and the original transmitted beam corresponds to $2L/c$, where c is the speed of light in the medium. This leads to an additional interference at the detector, which manifests itself as sinusoidal modulation in the spectrum with frequency $c/2L$ (Hz) [26, p. 193]. In order to prevent those modulations in the spectrum, transmissive optics usually are wedged, i.e. one surface is at a slight angle to the other.

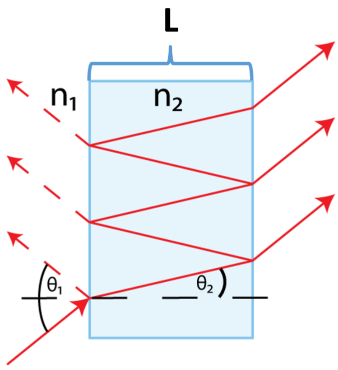

Figure 2.5.: Formation of etalons in a tranmissive optic. Part of a monochromatic light ray entering the medium with an angle θ_1 is reflected of the first boundary layer, which is repeated inside the medium at the second boundary layer. If this is repeated several times, the light rays exiting the optic will have different optical path lengths and thus create a characteristic sine wave effected by the thickness of the optic. A wedged window as a similar effect to the light entering at a specific angle of incidence θ_1. While multiple reflections still occur in the optic, they will exit at a different position to the main beam, which was transmitted first.

To summarize, the effect of finite retardation of the interferogram leads to finite resolution given by the ILS of the interferometer. The use of a stable reference laser, most commonly a stabilized HeNe-laser, enables the unknown signal to be sampled at precise intervals of retardation, eliminating the effects of varying mirror speed. While the combination of a laser as almost perfectly collimated source plus the use of retroreflectors compensates the problems posed by divergence and mirror tilt, while also enabling a high degree of control over alignment. Etalons introduce additional and often unwanted modulations in the spectrum and can easily be counteracted with wedged optics. The identification of etalons is instead a more tiresome and meticulous process.

2.3. Optical Frequency Combs for FTIR Spectroscopy

By switching from established incandescent sources to optical frequency combs (OFCs), a number of advantages can be gained in terms of wavenumber and photometric accuracy and precision (see 2.3.3). In order to obtain such an OFC, a mode-locked laser (see 2.3.1) has to be stabilized via precise control of its two defining frequencies f_{rep} and f_{ceo} (see 2.3.2).

2.3.1. Mode-locked Lasers

Since their advent in the 1960s [27], lasers have become an invaluable tool, as well as a active research area in science. Every laser consists of three basic elements, a pump, a gain medium, and a resonator. Basically the pump supplies energy to the gain medium, leading to population inversion of energy states and consequently to spontaneous emission of photons [26, p. 459]. The resonator, in turn, reflects some of those photons back towards the gain medium, leading to stimulated emission of photons which are exact copies of the stimulating photon. While constantly coupling light out of the cavity in the state of stable operation, a laser is said to run in continuous-wave (cw) mode. The other main mode of operation is to produce pulsed light, for which multiple methods exist, like Q switching for nanosecond pules, gain switching fro nanosecond to picosecond pulses, cavity dumping for nanosecond pulses and more [28]. The method relevant for this work is the process of mode locking, where all resonant modes in the cavity are in phase, creating a periodic series of femtosecond pulses [29]. In order to do so, an active modulator (e.g. acousto-optic or electro-optic modulators) or passive modulator (e.g. saturable absorbers or kerr lenses) is needed, which introduces a phase bias to the system prompting lasing with the desired phase relation [30]. The duration τ_{p} of such pulses is given by the round trip time T of the optical resonator with length L and the number of modes M, making it inversely proportional to the spectral bandwidth $\Delta\nu$ [26, p. 532]:

$$\tau_{\mathrm{p}} = \frac{T}{M} = \frac{2L}{c \cdot M} = \frac{1}{\Delta\nu} \tag{2.17}$$

A laser that operates in such a pulse operation is called a mode-locked laser. For any instant in time, its modes are narrow lines separated by a frequency

$$f_{\mathrm{rep}} = \frac{c}{2L} \tag{2.18}$$

from neighboring modes. The first resonator mode is offset from DC (0 Hz) by the so-called carrier-envelope offset frequency $f_{\mathrm{ceo}} < f_{\mathrm{rep}}$. Therefore the frequency of the n-th mode is completely described by [11]:

$$f_{\mathrm{n}} = n f_{\mathrm{rep}} + f_{\mathrm{ceo}} \tag{2.19}$$

Due to mirror vibrations, thermal drifts, noise in pump intensity and quantum noise, a single comb line exhibits a finite linewidth, also linked to timing and phase jitter of the pulse train [31].

Using such a source for a FTS already brings all advantages of a laser, although the spectrum is not as broad as for incandescent sources. The interferogram recorded by a FTS resembles the interferogram of a continuum source, with a clear centerburst at ZPD. The spectrum also resembles a continuum, as the drift of the comb modes makes a distinction between them impossible. In order to distinguish between two neighbouring comb modes, their drift and linewidth needs to be smaller than half the repetition rate of the modelocked laser.

2.3.2. Optical Frequency Combs

In order to obtain an OFC, a mode-locked laser needs to be stabilized. This requires precise control over the system, as to keep the repetition rate and the carrier-envelope offset frequency at constant values over long periods of time.

As the repetition rate of a modelocked laser is given by the effective length of the resonant cavity, one common solution to keep f_{rep} constant, is to modulate the cavity length thus counteracting frequency shifts via a feedback loop. After the laser cavity a photodiode can be used to directly measure f_{rep}, which is typically in the kHz-GHz range. By mixing one harmonic with a precisely known reference, a feedback loop drives piezoelectric transducers mounted on the back of the cavity mirrors, changing the effective cavity length [32]. It has to be noted, that an OFC with optical linewidths in the range of single Hz needs an optical reference for stabilization of f_{rep}, as the error from the stabilized mode to mode of interest increases with mode number squared [32].

While several levers in the system allow to control f_{ceo}, one common way is to modulate the pump current to counteract drifts. By doing so, one first needs to measure the carrier-envelope offset frequency. This is usually done via a so-called f-to-2f interferometer using second harmonic-generation [33], while for example other methods use difference-frequency generation [34]. In the f-2f interferometer, the signal is split into two parts, one of which is frequency doubled using second harmonic-generation inside a non-linear medium. By beating the frequency-doubled light with the original light at double the frequency the carrier envelope offset can be measured (see equation 2.20).

$$f_{\mathrm{ceo}} = 2f_{\mathrm{n}} - f_{2\mathrm{n}} = 2\left(nf_{\mathrm{rep}} + f_{\mathrm{ceo}}\right) - \left(2nf_{\mathrm{rep}} + f_{\mathrm{ceo}}\right) \tag{2.20}$$

An error signal is produced as response to changes in f_{ceo} that drives an acousto-optic modulator in the pump beam path, changing the intensity of the pump and thus the refractive index of the gain medium [35], [36]. The change in refractive index leads to a change in group and phase velocity, and thus f_{ceo}, as it can be expressed as the ratio of group to phase velocity inside the laser cavity [32]. The pump power modulation can also be controlled via the Kerr effect [37], [38], or by aligning the cavity to adjust the group-delay [33], [39].

Once the OFC is stabilized to an extent where noise and drifts are negligible over the measurement time, a comb mode resolved spectrum can be retrieved. The incoming wave consists of multiple spectral components with equal frequency intervals of f_{rep} (Hz), while the interferogram consist of a series of bursts separated by c/f_{rep} (m). An example is given in figure 2.6, where an OFC was simulated using equation 2.5. A repetition rate of 250 MHz and a carrier-envelope offset frequency of 50 MHz with mode numbers ranging from 200 000 to 200 500 were used. The modelled double-sided FTS has an optical scanning length of 4 m, centered around the centerburst at ZPD.

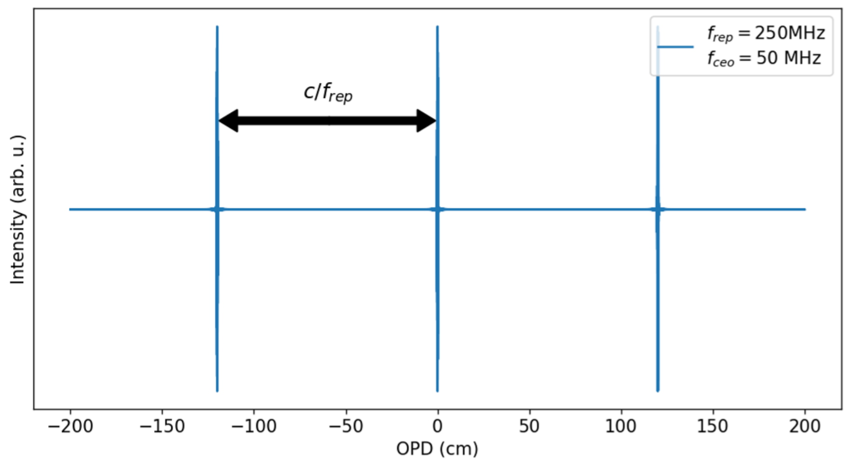

Figure 2.6.: Simulated interferogram from an OFC with $f_{\mathrm{rep}} = 250$ MHz and $f_{\mathrm{ceo}} = 50$ MHz. Due to the computing expenditure at optical wavelengths, the mode numbers were chosen as small as possible while still preserving the characteristic centerburst associated with broadband spectra. As such, the spectrum spans a width of roughly 15 nm centered around 5992.5 nm. The different bursts are separated by ≈ 119.9 cm as dictated by f_{rep}.

With sufficient resolution, a comb mode resolved spectrum is obtained, where the individual comb modes are separated by f_{rep}. Each mode can be interpreted as a delta function, convolved with the ILS. Assuming all comb modes have the same spectral intensity, the ILS contribution from all modes averages to a flat horizontal line [12]. If a narrow absorption feature smaller than f_{rep} attenuates a comb tooth, its ILS will become visible as the characteristic ringing of the sinc function, leading to a loss in photometric accuracy. In general the spectral sample points will also not overlap perfectly with the known comb mode positions, leading to inadequate wavenumber accuracy. Getting rid of these problems requires the precise matching of the OFC to the spectral sample points, which can be envisioned as overlapping the sample and OFC combs. If this is achieved, the ILS of the absorbed comb tooth has its zero-crossings exactly at the position of the other sample points, thus eliminating cross-talk between them. Not only is the photometric accuracy preserved, the wavenumber accuracy is improved to the linewidth of the comb modes, as one sample point on the spectrum has no other contributions and corresponds to one precisely known comb tooth given by 2.19.

2.3.3. Comparison of OFC to conventional sources in FTIR

Table 2.1 gives an overview of the advantages and disadvantages involved in using an OFC rather than a white-light source (WLS). OFCs stand out due to their high coherence properties compared to sources following thermal radiation, additionally high signal-to-noise ratios (SNR) can be achieved due to the higher spectral radiance [8], [9]. In general every laser source exhibits less divergence than a white light source, which limits the maximum retardation achievable in a FTS as indicated in equation 2.14. The discrete nature of an OFC together with the fixed spectral separation between the comb modes is its biggest advantage, as it directly leads to the linewidth limited resolution, whereas the best resolution attainable using a WLS is inherently limited by the ILS. The photometric and wavenumber accuracy for ILS-free spectra are orders of magnitude higher than for common incandescent sources.

OFC	WLS
high coherence	low coherence
high SNR	low SNR
low divergence	high divergence
discrete	continuous
linewidth limited resolution	ILS limited resolution
limited spectral width	thermal radiation
high engineering	low engineering
high cost	low cost

Table 2.1.: Comparison between OFC and WLS properties.

With the above mentioned advantages comes a set of disadvantages that have to be considered when using an OFC as source for a FTS. For applications where an especially broad spectrum is required, mode-locked lasers and thus OFCs are often inadequate as their spectral bandwidth is inversely proportional to their pulse duration. For example a

100 fs pulse has a spectral bandwidth of 10 THz, which corresponds to 33 nm for center wavelength of 1000 nm. In contrast the thermal radiation of a commercially available WLS (Thorlabs SLS401) spans from 240 to 2400 nm following the radiation of a 5800 K blackbody source. Finally the high engineering and high cost aspects of OFCs have to be considered, in comparison to the low costs of already established incandescent sources. As a mode-locked laser has to be highly engineered to stabilize f_{rep} and f_{ceo} to obtain an OFC, the additional time spent on design and maintenance is far greater than the simple use of a light bulb. Although OFCs are commercially available and thus eliminate the need for self-made stabilization, their costs far outweigh a commercial WLS.
As will be shown in 2.7, the methods to obtain a spectrum with sub-nominal resolution are solely computational and can be included in any setup that has access to an OFC.

2.4. Noise & Performance in FTIR spectroscopy

Deviations from the proper operation of the interferometer usually result in the addition of unwanted frequencies to the spectrum. The identification and subsequent reduction of such noise sources is an important task in any scientific environment and is in itself a versatile problem. Specific to a FTS are the problems of varying mirror speed and sampling at unequal increments of OPD. A sinusoidal variation in mirror speed will show as spectral sidebands around the center frequency following equation 2.8, whereas a random deviation results in white noise that is equally spread over the spectral region effectively decreasing the signal-to-noise ratio (SNR) [40].

Similarly, if the interferogram is sampled with different steps of retardation, including random deviations, random noise is added to the spectrum [19, p. 167]. As mentioned in 2.2, the usual way of sampling an unknown interferogram at equal steps of retardation evaluates to interpolation at the zero-crossings of a well known reference interferogram as firstly demonstrated in [24]. The method employed in chapter 3 differs from this approach, by direct compensation of any deviation in the reference laser spectrum, using the phase modulation property of the Fourier transform as given in 2.2.

Additionally, if the intensity of the signal varies as a function of time, so-called fluctuation noise will occur over the corresponding frequency range. In contrast to the sources of noise that occur due to sampling errors or mirror tilt, fluctuation noise is multiplicative [19, p. 169]. One common example where fluctuation noise plays a huge role, is the so-called 5 o'clock effect. Here the performance of a scientific instrument can increase after 5 p.m., because other sources of noise are being turned off, as the regular working hours come to a close. The best way to counteract this type of noise, is to choose the mirror speed in such a way, that the desired wavelengths are being sampled at frequencies far away from the frequencies of the noise sources [19, p. 170].

In order to give quantitative statements about noise in a FTS, so-called 100% lines are used. Two spectra, that were measured consecutively and under the same measurement conditions, are ratioed to one another and afterwards relative noise is measured as root-mean-square (rms) error of the ideally flat horizontal line with the value of 1. This gives information about the variation of noise across the spectrum with the SNR given as [19, pp. 181-183]

$$\mathrm{SNR} = \frac{100}{\text{rms noise}} \tag{2.21}$$

If there is a considerable delay between the two recorded spectra, the 100% line gives additional information about the variation of noise in time. In general it is good practice to record a 100% line directly after every major instrument calibration and store it permanently, in order to compare the performance over a long time period. Short-term measurements should be done before and after every serious measurement run, in order to ensure decent quality of the measured spectra [41]. In practice it is encouraged to have two permanent empty beam reference spectra stored from the last system calibration (Reference1 & Reference2), and record two empty beam spectra directly before and after the measurement of the desired sample (Test1 & Test2) [41].

The ratio of Test1 to Reference1 is referred to as the Energy-Spectrum-Test. It is used to categorize misalignment meaning that the modulation of the 100% line should not exceed $0.95 - 1.05$ [41]. High losses at higher wavenumbers are ascribed to interferometer misalignment and uniform losses can be ascribed to either vignetting or misalignment of non-interferometer optics. The classical 100%-Line-Test is to ratio Test2 to Test1, checking for short-term differences which could be linked malfunctions or external interference. Here the variation in the 100% line should not exceed 0.99 – 1.01 [41].

Finally, the Signal-Averaging-Test is used to verify that the SNR increases with the square root of the number of averages [41]. Two consecutive spectra are recorded for increasing number of averages, the corresponding spectra are ratioed and the SNR of their 100% line plotted as a function of averages. For each step of averages N with

$$N = 2^{2n}, \qquad n \in \mathbb{N}_0 \tag{2.22}$$

the noise should decrease by a factor of 2. This holds only for a limited number of averages, as long-term noise becomes a problem after a certain number of scans [41].

2.5. Digital Signal Processing

Broadly speaking, a signal is a physical quantity which changes as a function of independent variables [42, p. 3] over a period of time. Digital signal processing (DSP) concerns itself with the correct sampling (see 2.5.1) and quantization (see 2.5.2) of continuous signals and subsequent operations (see 2.5.3) on the discretely digitized signals [43, p. 4]. Consequently DSP is of utmost importance to all fields of science and technology (e.g. [44, pp. 6-22]), as every digitization of an analog signal adheres to its laws.

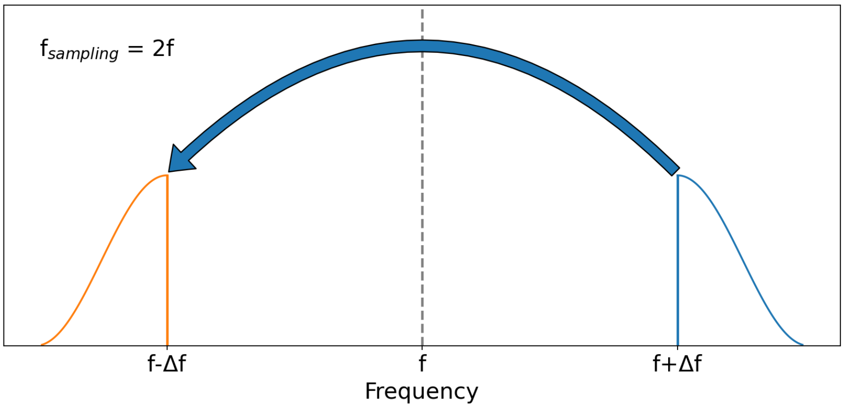

Figure 2.7.: Symmetric folding of feature at $f + \Delta f$ around Nyquist frequency f. Every frequency higher than half the sampling rate is mirrored to the corresponding lower frequency.

2.5.1. Sampling the Interferogram

A signal needs to be sampled with at least twice its own frequency, to reproduce it without loss of information and to avoid the effect of aliasing. This is known under the Nyquist criterion of digital signal processing, where unambiguous sampling is guaranteed [45]. The highest frequency that fulfills this criterion is called the Nyquist frequency f, depicted in figure 2.7 with the dashed line. All frequencies higher than this boundary are folded symmetrically around it, making signals of frequencies $f - \Delta f$ and $f + \Delta f$ overlap and any distinction between them impossible. To ensure that no such frequencies distort the spectrum, low-pass or band-pass filters are commonly used so that only the desired frequencies are sampled. Also the process of sampling a continuous signal with a constant frequency is identical to multiplying it with a series of Dirac delta functions, spaced by the sampling period. As a result, the spectrum repeats itself due to the convolution with the sampling comb. In a sense, aliasing can be understood as the overlap of high frequency components of the ever repeating spectrum [19, pp. 57-62].

As frequencies can also be expressed in wavenumbers, such a sampling is often given as being periodic in space, instead of time. If a specific resolution $\Delta\tilde{\nu}$ is desired for bandwidth $\tilde{\nu}_{\mathrm{BW}} = \tilde{\nu}_{\mathrm{max}} - \tilde{\nu}_{\mathrm{min}}$, the required number of points N becomes

$$N = 2\frac{\tilde{\nu}_{\mathrm{BW}}}{\Delta\tilde{\nu}} \tag{2.23}$$

which is identical to the formulation in terms of wavelengths $2\frac{\lambda_{\mathrm{BW}}}{\Delta\lambda}$, meaning that only signals with at least two samples per wavelength are correctly sampled.

A signal that is sampled at over a distance of $1/\Delta\tilde{\nu}$ cm, will have a spectrum consisting of points equally spaced by $\Delta\tilde{\nu}$ cm^{-1}. As described in 2.2, in FTIR it is paramount to sample at the same positions with regard to a reference laser for every measurement.

2.5.2. Dynamic Range & Analog to Digital Converters

An analog to digital converter (ADC) samples a signal corresponding to the Nyquist criterion, while quantizing the continuous amplitude of the signal into discrete bands, each of which is assigned a specific numerical value. Mostly binary numbers are used, evaluating to a number of quantization levels $N = 2^n$, for number of bits n. For 8 bits there exist 256 discrete amplitude levels, while for 20 bits there are 1048576 levels. For every increase in bit, the so-called dynamic range,

$$\mathrm{dB} = 20 \log \left(\frac{2^n}{2^0} \right), \tag{2.24}$$

which is the ratio of maximum to minimum measurable signal, increases by 6 dB [19, p. 64], [43, p. 8], as shown with

$$\Delta \mathrm{dB} = 20 \log \left(\frac{2^{n+1}}{1} \right) - 20 \log \left(\frac{2^n}{1} \right) = 20 \log (2) \approx 6 \tag{2.25}$$

While sampling the amplitude, it is important that the least or second to least significant bit is kept for sampling detector noise, as without, averaging would have no effect on the signal-to-noise ratio [19, pp. 65-67]. If the noise variation of the signal is much smaller than the least significant bit of the ADC, multiple measurements of the signal would always evaluate to the same result, thus the quantization noise for energy level ε is needed as the probability density $p(\varepsilon)$

$$p(\varepsilon) = \begin{cases} 1/Q & \text{for} \quad -Q/2 < \varepsilon < +Q/2 \\ 0 & \text{else} \end{cases} \tag{2.26}$$

with normalized width of quantization band $Q = 1/N$ [43, p.8]. In other words, the random noise of a single measurement must exceed the discretization introduced in analog-to-digital conversion. Otherwise averaging would not improve the accuracy of the measurement, as each analog value would be digitized as the exact same value. As an example, for a signal with a range of 4 V peak-to-peak, digitized at a resolution of 8 bit, the random noise must be on level of $4/2^8 = 0.156$ V. Due to it being independent of the sampling frequency, the digitization noise disperses over the entire bandwidth of the signal. While for the better part of the 20th century so-called sample-and-hold ADCs were used, since the 1990s [24] sigma-delta ($\Sigma\Delta$) ADCs have become the standard in FTIR spectroscopy. They are able to sample with a constant sampling rate up to several MHz using an internal reference [19, pp. 71-74]. After the signal was acquired, steps are taken computationally to switch from constant time to constant space sampling.

2.5.3. Averaging, Interpolation & Zero-Padding

Regarding correct signal averaging of interferograms, it is not only necessary to reserve the least or second to least significant bit for noise, also the position of the interferograms to each other has to be matched precisely [19, pp. 104, 106]. If the interferograms are sampled at equal steps of retardation and have the same number of points, but were sampled from different starting points, values at different retardations will be averaged, resulting in an untrue spectrum. To circumvent such problems, usually a peak finding algorithm locates the peak of broadband sources at ZPD and afterwards truncates the signal to a symmetric number of points around the peak intensity. The algorithm described in chapter 3 uses cross-correlation (see 2.6.1, equation 2.37) to find the overlap between two recorded interferograms and then shifts the second signal on top of the other one. One signal is resampled beforehand to the same points as the other and truncated to the correct length, in order to ensure signal averaging at correct retardation. As soon as the spacing of the sample points corresponds to steps of equal retardation, the signal can be resampled with arbitrary step size using linear or higher order splines. Higher frequency components that were lost during the analog-digital conversion can not be recovered. As for spectral interpolation, usually polynomial splines are used to estimate the spectrum between two sample points [19, p. 228]. Alternative to simple interpolation between spectral samples, is the process of zero-padding (also called zero-filling) the interferogram. For an interferogram of length N, the real and imaginary spectra are both of the same length, but by the addition of N zeros to both sides of the interferogram the number of points per resolution element is doubled, with the original points staying the same and the newly acquired points showing the ILS of the system [19, pp. 227-228].

2.6. Fourier Transform

The aim of this chapter is to provide a short but detailed theoretical overview of the FT and fast Fourier transform (FFT), together with the convolution and correlation integrals. Those are the necessary tools to understand the ILS-corrections described in 2.7. A short mathematical description of the classic complex Fourier transform is given below in 2.6.1 together with a list of important properties, establishing the foundation on which the fast Fourier transform builds itself in 2.6.4. The importance of the convolution and correlation theorems are highlighted separately in 2.6.2 and 2.6.3. Taking into account the complex nature of the Fourier transform, the relationship between the phase angle $\theta_{\tilde{\nu}}$, the magnitude spectrum and the true spectrum is explored in 2.6.5.

2.6.1. The Complex Fourier Transform and its Properties

The definitions of the classic Fourier transformation and its inverse counterpart are given in equations 2.27 and 2.28, while their properties are listed in table 2.2. Here functions in the frequency domain are written with uppercase letters with frequency f while functions in the time domain are written with lowercase letters, dependant on time t.

$$\mathcal{F}\{h\left(t\right)\}\left(f\right) = H\left(f\right) = \int_{-\infty}^{+\infty} h\left(t\right) e^{-2\pi i f t}\, dt \tag{2.27}$$

$$\mathcal{F}^{-1}\{H(f)\}(t) = h(t) = \int_{-\infty}^{+\infty} H(f)\, e^{2\pi i f t}\, df \tag{2.28}$$

The given properties in table 2.2 are reflected upon in the algorithms and measurements described in 3, like the existence of a zero-frequency component due to the DC-part of the interferogram, while also delivering the mathematical basis of the frequency correction algorithms in 2.7 via the time scaling and modulation properties in the time domain.

The first property in table 2.2 is essential to the concept of Fourier decomposition, as independent inputs can be converted to independent outputs [20, p. 42] and can be easily derived following integration rules. On the other hand, the second property can be derived by interchanging $h(t)$ in equation 2.28 with $h(-t)$ and switching the variables t and f [46, p. 32]. The scaling property and its inverse counterpart can be derived by substituting $t' = kt$ or $k' = kf$ respectively in equations 2.27 and 2.28 [46, pp. 32 - 35]. The second to last property will be encountered again in 2.6.5 and can be derived with substituting $t' = t - t_0$ in equation 2.28

$$\mathcal{F}\{h(t-t_0)\}(f) = \int_{-\infty}^{+\infty} h(t-t_0)\, e^{-2\pi i f t}\, dt \tag{2.29}$$

$$= \int_{-\infty}^{+\infty} h\left(t'\right) e^{-2\pi i f (t'-t_0)}\, dt' \tag{2.30}$$

$$= e^{-2\pi i f t_0} \underbrace{\int_{-\infty}^{+\infty} h\left(t'\right) e^{-2\pi i f t'}\, dt'}_{H(f)} \tag{2.31}$$

$$\tag{2.32}$$

resulting in

$$\mathcal{F}\{h(t-t_0)\}(f) = e^{-2\pi i f t_0} H(f) \qquad \square \tag{2.33}$$

The last property in table 2.2 can be derived in an analog way. It serves a key part in achieving sub-nominal resolution, by shifting the frequency scale of the FTS by f_{ceo}.

2.6.2. Convolution

The convolution integral as defined in equation 2.34 together with the convolution theorem in equation 2.35 are a cornerstone in the discussion of FTIR and have been encountered within the context of the ILS in 2.2.

$$y(t) = \int_{\mathbb{R}} h(\tau)\, x(t-\tau)\, d\tau = h(t) \star x(t) \tag{2.34}$$

Time domain	Frequency domain
Linearity $ax\left(t\right)+by\left(t\right)$	Linearity $aX\left(f\right)+bY\left(f\right)$
Symmetry $H\left(t\right)$	Symmetry $h\left(-f\right)$
Scaling $h\left(kt\right)$	Inverse scaling $\frac{1}{\lvert k\rvert}H\left(\frac{f}{k}\right)$
Inverse scaling $\frac{1}{\lvert k\rvert}h\left(\frac{t}{k}\right)$	Scaling $H\left(kf\right)$
Time shift $h\left(t-t_0\right)$	Phase modulation $H\left(f\right)e^{-2\pi i f t_0}$
Time Modulation $h\left(t\right)e^{2\pi i t f_0}$	Frequency shift $H\left(f-f_0\right)$

Table 2.2.: Properties of the Fourier transform; given to the left are the properties in the time domain together with the corresponding properties in the frequency domain to the right [20, pp. 57-63], [46, p.31-46].

$$h\left(t\right)\star x\left(t\right)\Longleftrightarrow H\left(f\right)\ X\left(f\right) \tag{2.35}$$

$$h\left(t\right)\ x\left(t\right)\Longleftrightarrow H\left(f\right)\star X\left(f\right) \tag{2.36}$$

The theorem states, that the Fourier transform of the convolution of two functions, is the multiplication of the Fourier transforms of said functions [47, p. 31]. This is a powerful tool, as it explains the rather abstract idea of convolution, with a multiplication viewed from a different angle. It also massively simplifies the computation of a convolution integral, by switching to the other domain, multiplying the Fourier transforms and switching back to the original domain, rather than computing the integral or solving it analytically. Most importantly, convolution and its effects give insight into the instrumental line shape and apodization as originally discussed in 2.2, where a rectangular acquisition function always leads to a convolution of spectral samples with the sinc function [20, p. 51].

Independent from the finite retardation, the signal also gets sampled corresponding to the Nyquist criterion as in 2.5.1, which discretizes the signal. Sampling can be viewed as a multiplication of the finitely long signal with a train of equally spaced delta functions. Those multiplications in the time domain are reflected as convolutions in the frequency domain. The FT of the boxcar acquisition function, which corresponds to the ILS, is given in equation 2.13, whereas the FT of the series of delta functions equally spaced by time T becomes another train of delta functions equally spaced by $1/T$. Together, each delta function in the frequency domain, gets convolved with the ILS resulting in a series of equally spaced sinc functions, which add up at all positions.

2.6.3. Correlation and Coherence

On the other hand the correlation integral and its theorem are given in equations 2.37 and 2.38, serving as a quantitative way of determining coherence (long-term phase relationships) between two signals, ranging from zero (incoherent) to one (coherent) [47, p. 194]. If the two signals are different functions the term cross-correlation is used, whereas the term auto-correlation is used if the functions are the same.

$$z(t) = \int_{\mathbb{R}} h(\tau)\, x(t+\tau)\ d\tau \tag{2.37}$$

$$\int_{\mathbb{R}} h(\tau)\, x(t+\tau)\ d\tau \Longleftrightarrow H(f)\ X^*(f) \tag{2.38}$$

Correlation and thus coherence are fundamental in the description of interferometers, as a high degree of temporal coherence between beams in the interferometer arms is necessary [47, p. 196] in order to retain the interferogram modulation over long intervals of retardation, without noise overtaking the signal.

Consider the two beams propagating in the two arms of a Michelson interferometer. The delay between the beams can be expressed as time $\tau_{\mathrm{d}} = \delta/c$ with retardation δ and the speed of light c. Immediately after an incoming polychromatic beam is split into two, there exists a strong correlation between the beams, expressing a long-term phase relationship. In fact, correlation and coherence are indistinguishable in this context, as the former serves merely as quantification of the latter [47, p. 195, 221]. If no inherent phase relationship between the spectral components exist, they will loose their mutual predictability and thus coherence/correlation over time. The amount of time which needs to pass, before the phase relationship loses this predictability, is defined as the coherence time $\tau_{\mathrm{c}} \approx \frac{1}{\Delta\nu}$ with frequency bandwidth $\Delta\nu$ [26, p. 354], [47, p. 205]. Note that this expression is identical to the pulse duration of an OFC as in equation 2.17.

For a temporal delay $|\tau_{\mathrm{d}}|$ bigger than the coherence time, the compared signals are considered to have become incoherent. Full coherence is only given for $|\tau_{\mathrm{d}}| = 0$. Every state between that is considered to be partially coherent and can, as stated before, be expressed quantitatively by the correlation function [47, pp. 204-209]. Considering a Michelson interferometer, a phase delay is voluntarily introduced to one interferometer arm, which for broadband sources lead to the centerburst and the rapidly decaying envelope of the interferogram. At ZPD, the two beams are completely coherent, as their phase relationship is maintained. The decaying envelope diminishes the modulation to zero as soon as the time delay between the beams reaches the coherence time [47, p. 209]. After the coherence length, which is the length light travels during one coherence time, any further increase in retardation does increase the resolution, but does not add spectral information, as only noise is recorded.

This can further be illustrated by looking at the intensity at the detector for two interfering waves U_1 and U_2. Their intensities are given by their average squared magnitude $I_{1,2} = \langle |U_{1,2}|^2 \rangle$, and their normalized cross-correlation is given by

$$g_{12} = \frac{\langle U_1^* U_2 \rangle}{\sqrt{I_1 I_2}} \tag{2.39}$$

which is used to express the intensity at the detector as

$$I = I_1 + I_2 + 2\sqrt{I_1 I_2} |g_{12}| \cos(\varphi) \tag{2.40}$$

where φ corresponds to the phase of g_{12} [26, p. 359]. It is immediately clear, that as soon as the cross-correlation term $|g_{12}|$ reaches zero, the modulation and thus all interference is lost. From this the so-called fringe visibility $\mathscr{V}$, or modulation efficiency

$$\mathscr{V} = \frac{I_{\max} - I_{\min}}{I_{\max} + I_{\min}} = \frac{2\sqrt{I_1 I_2}}{I_1 + I_2} |g_{12}| \tag{2.41}$$

can be defined, which is a function decreasing as the envelope of the interferogram decreases, reaching zero with the coherence time τ_c [26, p. 360] [47, p. 209].

In practice the modulation of the interferogram is only completely lost for infinitely long retardation, as the decaying envelope approaches zero [3, pp. 227-228], although the added noise will overshadow the remaining modulation. This is why high resolution white light interferometers, like the Bruker IFS 125HR that can reach resolutions below 0.0009 cm^{-1}, take considerable time to average recorded spectra. For example, a spectrum is advertised with 0.0011 cm^{-1} resolution, which had to be recorded over a period of ten hours [23, IFS 125HR Flyer EN].

Other uses of the correlation integral can be included in signal processing, for example to enable correct signal averaging. As two separately recorded interferograms will have a correlation maximum at the centerburst, they can be truncated and resampled to the precise same positions as is mentioned in 2.5.3 and 3.2.

2.6.4. Fast Fourier Transform

The basis of the fast Fourier transform algorithm and in fact all computer-based FTIR spectroscopy builds on top of the discrete complex Fourier transform (DFT) of N points [19, p. 79]

$$B(\tilde{\nu}_i) = \sum_{k=0}^{N-1} S_0(k)\, e^{-2\pi i \tilde{\nu}_i k/N}, \qquad \tilde{\nu}_i = 0, 1, 2, \ldots, N-1 \tag{2.42}$$

which is equivalent to $N-1$ summations and N multiplications for one wavenumber $\tilde{\nu}_i$ and with N terms of $\tilde{\nu}_i$ equating to a complete set of N^2 multiplications and $N(N-1)$ additions . As the discrete Fourier transform only approximates the continuous form, equivalence is only given if certain criteria are matched. The time signal has to be a periodic, band-limited function that fulfills the Nyquist criterion, where the boxcar acquisition function is non-zero for one period of the time signal [46, p. 102]. For example, if the recorded interferogram is not recorded symmetrically, it will not be periodic due to discontinuities. The effect of which was mentioned in 2.2 as leakage. This constitutes that the DFT is a special case of the continuous Fourier transform, meaning that the properties described in table 2.2 as well as correlation and convolution are also valid for the discrete version [46, p. 123]. Subsequently FFT is simply a way to calculate the DFT efficiently, reducing the computation time drastically by using matrix factorization. The parameter W in equation 2.43 is used in order to rewrite the above equation into a new form

$$W = e^{-2\pi i/N} \tag{2.43}$$

$$B(\tilde{\nu}_i) = \sum_{k=0}^{N-1} S_0(k) W^{\tilde{\nu}_i k}, \qquad \tilde{\nu}_i = 0, 1, 2, \ldots, N-1 \tag{2.44}$$

This sum can now be expressed by expressing $B(\tilde{\nu}_i)$ and $S_0(k)$ as vectors together with the matrix $\mathbb{W}$ and the cyclical properties

$$W^0 = 1 \tag{2.45}$$

$$W^{\tilde{\nu}_i k} = W^{\tilde{\nu}_i k \mod N} \tag{2.46}$$

$$W^{k+N/2} = -W^k \tag{2.47}$$

of the elements in $\mathbb{W}$ can be used to simplify it further [19, p. 80].

These simplifications follow the Cooley-Tukey algorithm which can be applied to any number of N, but this short description restricts itself on the case $N = 2^\gamma$, with $\gamma \in \mathbb{N}$. By factorizing the $N \times N$ matrix $\mathbb{W}$ into γ matrices with same dimension, and each matrix using the cyclical properties as outlined above to minimize the number of additions and multiplications, the FFT algorithm greatly reduces the amount of performed calculations [46, pp. 151-152]. As a result, the number of additions is reduced to $N\gamma$ and the number of multiplications to $N\gamma/2$. With the dominating factor being the complex multiplications, the ratio of directly computing the DFT to computing it via the FFT evaluates to

$$\frac{N^2}{N\gamma/2} = \frac{2N}{\gamma} \tag{2.48}$$

meaning that the direct way needs to compute $\frac{2N}{\gamma}$ times more multiplications than the FFT [46, pp. 151-152]. For example, the FFT of an array with $N = 2^{20} = 1048576$ samples is 131072 times faster than just evaluating the DFT.

2.6.5. Phase Correction

The complex Fourier transform of the interferogram results in a complex spectrum $B'(\tilde{\nu})$, as already mentioned at the end of 2.1.1, consisting of a sine and a cosine parts. The sine components stem from asymmetries introduced to the interferogram, due to an ever slightly changing source intensity, a wavelength depending ZPD due to dispersion or a failure to precisely sample the interferogram at ZPD [20, pp. 101-102]. The complex wavenumber dependent phase angle $\theta_{\tilde{\nu}}$ arises from the asymmetry induced phase errors [20, pp. 102-107] and can be used to express the complex spectrum as

$$B'(\tilde{\nu}) = |B(\tilde{\nu})| e^{i\theta_{\tilde{\nu}}} \tag{2.49}$$

where $|B(\tilde{\nu})|$ is the magnitude spectrum and $e^{i\theta_{\tilde{\nu}}}$ the exponential modulation function [19, p. 85], [20, p. 47]. The true spectrum however is also a real function and not identical to the magnitude spectrum. It can be reconstructed by rearranging the above expression to

$$B(\tilde{\nu}) = B'(\tilde{\nu}) e^{-i\theta_{\tilde{\nu}}} \tag{2.50}$$

which corresponding to table 2.2 is identical to a shift in the time domain. The phase angle can be calculated as

$$\theta_{\tilde{\nu}} = \frac{\Im\{B'(\tilde{\nu})\}}{\Re\{B'(\tilde{\nu})\}} \tag{2.51}$$

the fraction between imaginary and real part of the complex Fourier transform [19, pp. 85-86], [20, p. 47]. This serves as way to correct the spectrum of double sided interferograms, whereas for single-sided interferograms other algorithms need to be employed like the Mertz method [48], or the Forman method [49].

2.7. Sub-nominal Resolution

By using an OFC as source for a FTS, a collection of processing steps can be performed, in order to match the frequency scale of the FTS with the scale of the OFC. This in turn guarantees that the spectral sample points assigned to the comb modes do not carry any contribution from neighbouring modes. If applied correctly and with sufficient stability of the OFC, the nominal resolution, dictated by the maximal OPD of the interferogram, can be neglected and the spectral resolution improved to the linewidth of the individual comb modes. To achieve this sub-nominal resolution, a series of prerequisites (see 2.7.1) has to be met, afterwards the frequency scale corrections can be applied (see 2.7.2, 2.7.3) leaving the spectrum with some slight deviations and errors as described in 2.7.4.

By restricting the constant space sampled interferogram of the OFC to a size equal to c/f_{rep}, the frequency sample spacing becomes f_{rep} [12]. Correcting for the carrier envelope offset f_{ceo} and remaining numerical differences, one frequency sample corresponds precisely to one comb line of the OFC. As a result, the zero-crossings of the ILS of a single sample point, are also spaced by f_{rep} and appear at the positions of all other comb lines as is illustrated in figure 2.8. Every comb line is thus completely free of influence from the other lines, and if one sample point shows absorption, only the corresponding comb line (given precisely by equation 2.19) can be responsible. By slightly changing f_{ceo} or f_{rep}, one can scan over an absorption feature and interleave the acquired spectra. The resolution is in theory then only given by the precise knowledge and stability of the OFC, which can in the optimal case be in the single Hz range. In practice, the most limiting factor is f^0_{FTS} which is determined by the accuracy of λ_{ref} (see 2.7.4) [13], which suffers from various effects acting on the interferometer such as those discussed in 2.2.

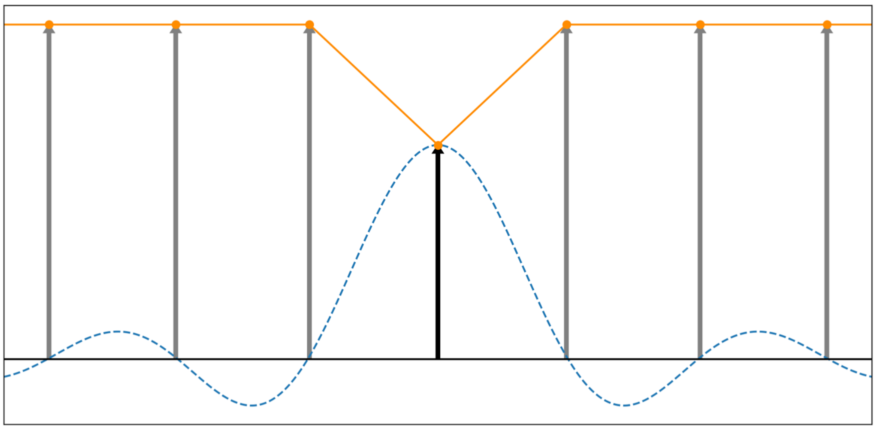

Figure 2.8.: ILS-free frequency comb spectrum with absorption line (black arrow); the contribution of the ILS (blue dashed) to the other comb lines is zero, as the maximal retardation is precisely matched to $\Delta_{\max} = \frac{c}{f_{\mathrm{rep}}}$; every sample point (orange) in the frequency domain consists of precisely one comb mode (grey arrows) and the resolution is governed by the positional knowledge of the frequency lines.

2.7.1. Prerequisites

As described in the previous sections, the interferogram of a stable frequency comb as in 2.3, has to be sampled at equal steps of retardation, equalling a constant number of times q per reference laser wavelength λ_{ref}. During the acquisition, the OFC has to be stable enough that two different comb lines never get sampled as one, meaning that one individual comb line must not vary by more than half the repetition rate. As the spectral resolution is given by the length of the acquisition boxcar function as described in 2.6.1, the frequency spacing of the sample points can be changed to f_{rep} by cutting the interferogram to a length given by $\Delta_{\max} = c/f_{\mathrm{rep}}$ [12]. The link between the length of the interferogram and the change in spacing in the frequency domain is a fundamental property of the Fourier transform, displayed in the third row of table 2.2.

As a discrete interferogram can not take on any length, a rounding error is introduced and the frequency scale of the FTS is given by the frequency f_{FTS}^{0},

$$f_{\mathrm{FTS}}^{0} = \frac{c}{\Delta_{\max}} = \frac{qc}{2\lambda_{\mathrm{ref}} N_0} \tag{2.52}$$

resulting in an interferogram with N_0

$$N_0 = \mathrm{round}\left(\frac{qc}{2\lambda_{\mathrm{ref}} f_{\mathrm{rep}}}\right) \tag{2.53}$$

points to each side of the centerburst [13].

After FFT, the spectrum contains N_0 points between frequencies ranging from 0 to $qc/2\lambda_{\mathrm{ref}}$. It is important to note, that precise knowledge of the OPD at every sample point is required, to ensure constant spacing and knowledge of f_{FTS}^{0}. The relative difference between the nominal resolution resulting from the truncated interferogram and the repetition rate can be expressed as ε_0 [13]

$$\varepsilon_0 = \frac{f_{\mathrm{FTS}}^{0} - f_{\mathrm{rep}}}{f_{\mathrm{rep}}} \tag{2.54}$$

By assigning every sample point frequency to an integer spaced by the nominal resolution f_{FTS}^{0} and comparing the resulting scale to the OFC as defined in equation 2.19, two problems can be identified: First the OFC is shifted by f_{ceo} and second the difference between f_{rep} and f_{FTS}^{0} leads to an increasing difference in the slopes of the scales for higher index n in equation 2.19. The solutions for these issues are discussed separately below.

2.7.2. Correction for Local Comb Mode

In order to correct for the shift by f_{ceo}, the sixth property of the Fourier transform in table 2.2 is used, where a modulation in the time domain leads to a shift of the sampling points in the frequency domain. The correction for f_{ceo} is thus easily achieved by multiplying the interferogram at every retardation δ with a modulation function [12], [13]

$$\exp\left(-2\pi i f_{\mathrm{ceo}} \delta / c\right) \tag{2.55}$$

Using this approach, the frequency scale can be shifted further in a way, as to be in exact local agreement for a desired comb mode n_{opt}:

$$f_{\mathrm{shift}}^{0} = -n_{\mathrm{opt}}\left(f_{\mathrm{FTS}}^{0} - f_{\mathrm{rep}}\right) = -n_{\mathrm{opt}} \varepsilon_0 f_{\mathrm{rep}} \tag{2.56}$$

As a consequence the difference between the OFC scale and the sampling point frequency scale is lowered to $(n - n_{\mathrm{opt}})\, \varepsilon_0 f_{\mathrm{rep}}$, with the benefit of being a simple and quick calculation [13].

2.7.3. Correction for Large Intervals of Comb Modes

While the method above delivers excellent local agreement between the frequency scales, the mismatch increases with difference $n - n_{\mathrm{opt}}$, leading to errors for broad spectra. In order to reduce this effect, the slope of the sampling scale can be changed by zero-padding the interferogram before FFT [12], [13]. The addition of $k_{\mathrm{pad}} N_0$ zeros on both sides of the interferogram changes the frequency spacing by $f^0_{\mathrm{FTS}} / (k_{\mathrm{pad}} + 1)$, as given by the time scaling property of the Fourier transformation given in table 2.2. By adding N zeros to both sides of the interferogram the frequency spacing corresponding to the comb modes changes and becomes f_{FTS} with corresponding relative difference ε [13]:

$$N = \mathrm{round}\left(\frac{qc}{2\lambda_{\mathrm{ref}} f_{\mathrm{rep}}} (k_{\mathrm{pad}} + 1)\right) \tag{2.57}$$

$$f_{\mathrm{FTS}} = \frac{qc}{2\lambda_{\mathrm{ref}} N} (k_{\mathrm{pad}} + 1) \tag{2.58}$$

$$\varepsilon = \frac{f_{\mathrm{FTS}} - f_{\mathrm{rep}}}{f_{\mathrm{rep}}} \tag{2.59}$$

In order to find the best match between f_{FTS} and f_{rep}, the optimal value of k_{pad} has to be found. Finding the correct integer value of k_{pad} reduces to finding the minimum value of $|\varepsilon|$ with respect to k_{pad}, with an example of this function visible in figure 2.9. The closer the nominal frequency of the FTS is to f_{rep}, the higher values of k_{pad} are needed to further decrease their discrepancy. By padding the interferogram with N zeros to both sides, $(k_{\mathrm{pad}} + 1)$ points get added between two comb lines which sample the ILS between the modes [13].

As drawback, the process of zero-padding and the FFT needed for the spectrum takes considerable computing time, as the size of the interferogram increases drastically. Using lower values for k_{pad} is preferable and can be combined by the shift procedure before padding as in the former section, using the new discrepancy between the scales the shift frequency becomes [13]

$$f_{\mathrm{shift}} = -n_{\mathrm{opt}} \varepsilon f_{\mathrm{rep}} \tag{2.60}$$

Together with the correction for f_{ceo}, the comb mode sample point spacing finalizes to

$$f^{\mathrm{n}}_{\mathrm{FTS}} = n f_{\mathrm{FTS}} + f_{\mathrm{ceo}} + f_{\mathrm{shift}} \tag{2.61}$$

The remaining differences between the sampling scale and the OFC scale evaluates to $(n - n_{\mathrm{opt}})\, \varepsilon f_{\mathrm{rep}}$ [13]. As the padding of the interferogram increases the number of points, it adds sampling points between the resolution elements of the comb modes. The actual spacing after the FFT for all points in the spectrum evaluates to the fraction $f_{\mathrm{pad}} = f_{\mathrm{rep}} / (k_{\mathrm{pad}} + 2)$, with every $(k_{\mathrm{pad}} + 2)$-th point being equal to a comb mode as sketched in figure 2.10.

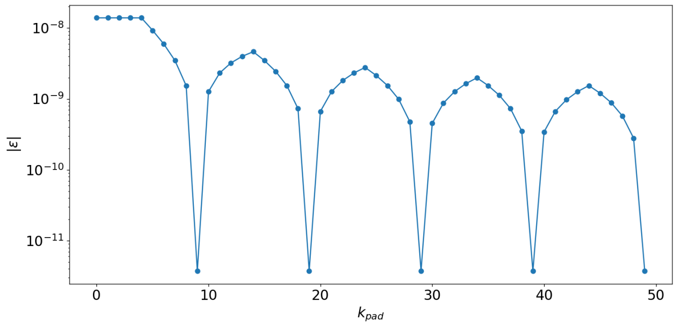

Figure 2.9.: Simulation of relative discrepancy $|\varepsilon|$ as function of k_{pad} with respect to a f_{rep} of 132 MHz sampled with maximal OPD of 400 centimeters with four samples per reference laser wavelength $\lambda_{\text{ref}} = 632.8$ nm; note the logarithmic ordinate axis.

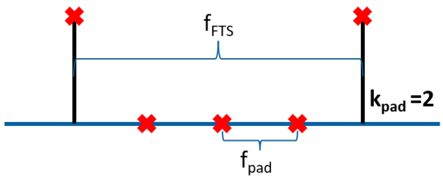

Figure 2.10.: Effect of padding an OFC interferogram with $N\,(k_{\text{pad}} + 1)$ zeros, for $k_{\text{pad}} = 2$. The vertical black lines depict two adjacent comb modes, the red crosses visualizing the sampling points of the spectrum. While the comb modes are spaced by f_{FTS}, the actual points in the spectrum are spaced by f_{pad}.

2.7.4. Accuracy of the Reference Laser and Residuals

As mentioned at the beginning of 2.7, the main factor of error corresponding to the above mentioned methods, is the precise knowledge of f^0_{FTS} dependant on λ_{ref}, as f_{rep} can be stabilized to high degrees [32]. If λ_{ref} is known with accuracy η the wavelength used by the FTS is given by $\lambda'_{\text{ref}} = (1 + \eta)\,\lambda_{\text{ref}}$, resulting in a dependence of the relative discrepancy ε on the accuracy of the reference laser [13]

$$\varepsilon = \frac{f_{\text{FTS}}}{(1+\eta)\,f_{\text{rep}}} - 1 \tag{2.62}$$

[13] also showed, that the remaining ILS distortion due to the mismatch of the frequency scales can be used as a reference to iteratively decrease η until the said distortion is below the noise baseline. For an ILS-free spectrum the accuracy of the reference laser has to be better than a certain limit η_{lim} which can be determined for an absorption line at mode position n_{abs} with signal-to-noise ratio SNR

$$\eta_{\text{lim}} = \frac{1}{\text{SNR}\; n_{\text{abs}}} \tag{2.63}$$

3. Experimental Setup and Results

In this chapter the setup of the FTS is described (3.1), as well as the data flow through our acquisition, processing and correction algorithm (3.2). The performance of the instrument is discussed in 3.3, with various metrics being presented and discussed. Finally, in 3.4, interferograms of an OFC, which were kindly provided by Prof. Piotr Masłowski PhD, of the Faculty of Physics, Astronomy and Informatics at the Nicolaus Copernicus University in Toruń, are processed with our algorithms to be ILS-free.

3.1. Spectrometer Design & Components

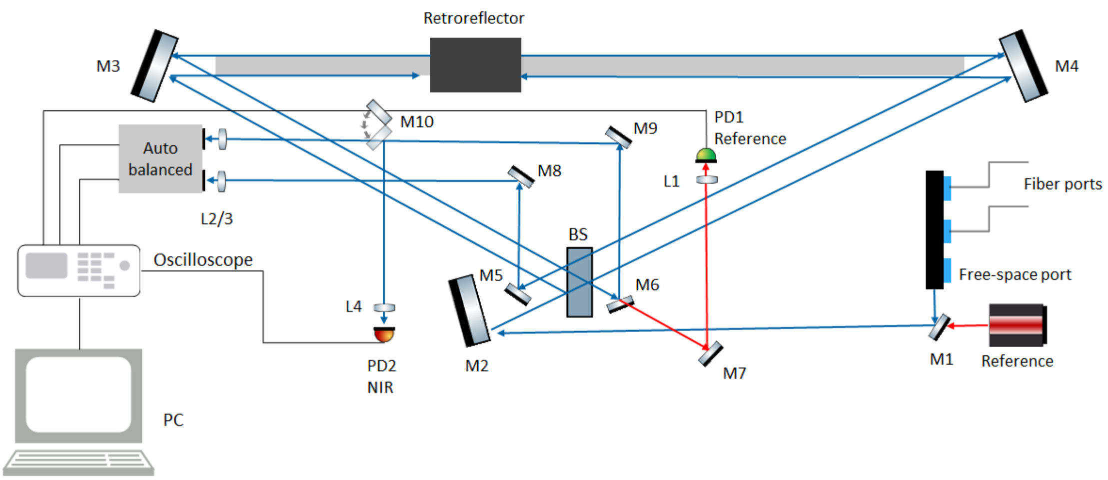

Figure 3.1.: Schematic of the FTS setup, consisting of optical cage system with fiber and free space ports, a frequency-locked cw reference laser, a pair of mirrors (M1 and M2) to couple into the interferometer consisting of a beamsplitter (BS), two mirrors (M3 and M4) and two retroreflectors mounted on a moving stage. Output signals are picked up using mirrors M5, M6 and M7. Whereas the output of the reference laser is send to the focusing lens L1 and to photodiode PD1, the infrared signals are directed via mirrors M8 and M9 to either the lenses L2, L3 and the auto-balanced mid-IR detector, or via flip-mirror M10 to focusing lens L4 and a NIR photodiode PD2. The detectors are linked to an oscilloscope which in turn is connected to a PC.

Instead of the classical Michelson-design depicted in figure 2.1, we opted for a double folded design, where two retroreflectors are mounted with their backs to one-another on a platform, which can be moved using a one meter long linear actuator (Aerotech ACT115DL) [50]. In contrast to the classical design as outlined in 2.1.1, both interferometer arms experience a shift in path length, effectively doubling the OPD of the system from two meters to four meters. This also doubles the Fourier frequency

$$f_{\tilde{\nu}} = V_{\mathrm{o}}\tilde{\nu} = 4V_{\mathrm{m}}\tilde{\nu} \tag{3.1}$$

as the optical velocity V_{o} is four times the velocity of the moving mirrors V_{m}.

As of writing this thesis, we unfortunately have to report that we lack an OFC in the laboratory. Our mode-locked laser currently misses the required stabilization mechanisms, leading to Piotr Masłowski, PhD and Dominik Charczun, MSc kindly providing some measurements, associated to their work on dual-comb cavity ring-down spectroscopy [51], [52]. Nevertheless the setup can be used for every appropriate source. The laser sources connected to the system are an in-house made mode-locked Ytterbium-based fiber laser centered around 1030 nm, with a repetition rate of 132 MHz as well as a commercial MIR quantum cascade laser (Thorlabs QF4550CM1) [53]. Both are already fiber-coupled once they enter the setup. The reference laser is a frequency locked fiber-coupled cw laser at 1532.8323 nm, which is used in the optical spectrum analyzer Redstone OSA305 from Thorlabs [21]. A free-space input port gives additional flexibility regarding possible sources being used.

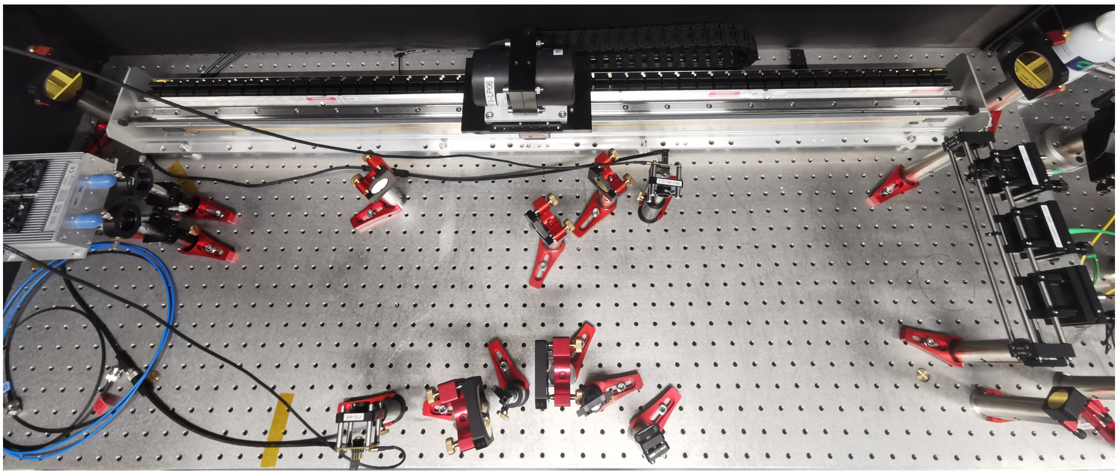

Figure 3.2.: Photograph taken from the setup in the laboratory. On the right-hand side the cage system is visible, with a connected NIR-fiber (top) a connected MIR-fiber (middle) and a red 635 nm laser module (Thorlabs CPS635R, bottom).

The collimation packages (Thorlabs F260APC-1064 and Thorlabs F028FC-4950) are mounted in two kinematic mounts, connected to an optical cage system. Drop-in mirrors (Thorlabs PF10-03-M02) are used to couple the desired signal into the system. The outgoing beam is reflected at mirror (M1, Thorlabs PF10-03-M02) and made to propagate in parallel to the reference laser, while being displaced laterally by roughly 1". The fiber coupled reference laser is connected to a collimation package (Thorlabs F260APC-1550) and mounted on a kinematic mount to the right of the optical cage system. In figure 3.1 the reference laser is shown in red, while the path of the signal beam is shown in blue. Where they propagate colinear, only the blue signal beam is depicted. A 2" mirror (M2; Thorlabs PF20-03-M02) couples the light into a CaF_2 plate beamsplitter (BS; Thorlabs BSW521) that is oriented 90 degrees to a moving stage. Each the reflected and transmitted beam hit another 2" mirror (M3, M4, both Thorlabs PF10-03-M02) close to the linear actuator, such that they reflect the rays parallel to the direction of the stage movement. The retroreflectors (Edmund Optics 49674) moving on the stage reflect all incoming light in parallel, but diagonally displaced.

The beams of both interferometer arms are consequently reflected back to the beamsplitter, where two interference patterns are produced. Starting with the balanced output, each arm experiences transmission and reflection, whereas the light at the unbalanced output experiences just reflection or transmission with regard to the beamsplitter, depending on the interferometer arm. Two D-shaped mirrors (M5, M6; both Thorlabs PFD10-03-M02) are placed closely to the beamsplitter in order to reflect the two outputs to two additional 1" mirrors (M8, M9, both Thorlabs PF10-03-M02) which send the light to a set of lenses (L2, L3; both Thorlabs LA5315-E) which focus onto an auto-balanced HgCdTe MIR detector (Vigo NIPM-I-5). Additionally, the balanced output of the reference laser is separately reflected (M7, Thorlabs PF10-03-P01) and focused using a lens (L1, Thorlabs LA1074-C-ML) on a photo-diode (PD1; Thorlabs PDAPC4), which is easily achievable due to the lateral displacement of the reference and signal beams. For NIR sources, a 1" mirror (M10, Thorlabs PF10-03-M02) is placed at a flip-mount which then sends the balanced output of the signal to a focusing lens (L4; Thorlabs LA1074-C-ML) and a NIR photo-diode (PD2; Thorlabs PDAPC4).

The detector PD1 of the reference laser is connected to the first channel of an oscilloscope (National Instruments PXI-5922), while the second channel can be switched to either the balanced or auto-balanced signal of the MIR detector, or the balanced signal of the NIR detector PD2. In turn the oscilloscope is connected to a PC with the developed software for data acquisition and spectrum retrieval. The interference fringes are sampled with the start of the measurement, initiated with the movement of the retroreflectors on the linear actuator.

3.2. Code Design and Data Flow

The main challenge in the development of the acquisition software, was the huge quantities of data collect over an entire scan, due to the large possible OPD length of the above described spectrometer. In order to improve the duty cycle efficiency of the instrument, the data acquisition and processing code is split into three threads, each executing concurrently to the others. This is illustrated in figure 3.4 a), after the first scan is finished and the oscilloscope stops acquisition, the data from the reference and signal channel are queued to the so-called calibration thread. While the next scan is initiated the data flows through the calibration thread and is then queued to the so-called processing thread. As soon as a thread finishes it looks for more data in the queue, only stopping if a predefined number of averages has been reached. After all threads finish execution, the data can be saved, or in the case of an OFC, be corrected for the ILS. A screenshot of the developed graphical user interface is presented in figure 3.3.

3.2.1. Scan Thread

Before acquisition starts, the user has to input the desired travel range of the retroreflectors, from start to stop. Any position from 0 to 1000 mm can be chosen as start point, with start $<$ stop. The number of averages is preset to one, resulting in repeated measurements without adding interferograms. This as well as the coupling of the oscilloscope, its voltage range and the apodization window used can be changed via the user interface. By clicking the start button, the scan thread starts as in figure 3.4 b).

First the program connects to the motion controller of the stage, waiting for input. Built-in motion commands written in C have been wrapped in Python and are forwarded to the controller. After automatically moving the mounted mirrors on the axis to the reference point at its center, a motion command issues a request to move to the starting position Pos1. Here an oscilloscope session is initiated, with sampling frequency chosen, as such that the reference laser is sampled four times per wavelength. With acquisition starting, the stage moves to the end point Pos2. Due to a severe frequency depended amplitude and phase response of the oscilloscope for sampling higher than 1MS/s, the mirror speed was chosen carefully, so that the calculated sampling for the highest Fourier frequency as in equation 3.1 doesn't exceed this limit. After the scan is finished, the acquired data is put in the calibration-queue effectively starting the calibration thread. If the number of scans is smaller than the number of desired averages, the stage receives another order to move to Pos1 starting acquisition anew until all required interferograms have been recorded.

3.2.2. Calibration Thread

The calibration thread shown in figure 3.4 c) is responsible for the transition from constant time to constant space sampling as well as correct signal averaging between scans. As soon as the queued data enters the thread, the first calibration process starts. Due to the mirror velocity slightly varying around its setpoint the interferograms are squashed and stretched, such that interpolation to constant space sampling is not possible. In order to correct for this we follow an algorithm developed by [54]. The FFT of the reference interferogram is performed and the maximum of the resulting frequency spectrum determined. Using the frequency shift property of the FFT as given in table 2.2, we can retrieve the phase modulation function of the reference interferogram by shifting the carrier frequency to zero and then performing the inverse FFT. We calculate the phase as a sum of phase carrier and phase modulation and can further calculate the linear phase simply by constructing a linearly sampled array from zero to the maximum of the aforementioned phase. The sample spacing thus corresponds to a natural fraction of the reference carrier frequency. Finally the signal and reference interferograms are linearly interpolated at the positions of the linear phase and passed to a routine determining speed thresholds of the stage, cutting the interferogram to exclude positions of accelerating mirror speed. The trimmed interferograms are calibrated again and afterwards the cross-correlation, as in equation 2.37, of the signal interferogram with previously recorded and averaged interferograms is calculated. The index of highest correlation is determined and the newly acquired array is shifted, interpolated and lastly added to the averaged signal. The averaged interferogram is then put to the processing-queue and like the scan thread, a logic gate determines whether to continue the thread or terminate it.

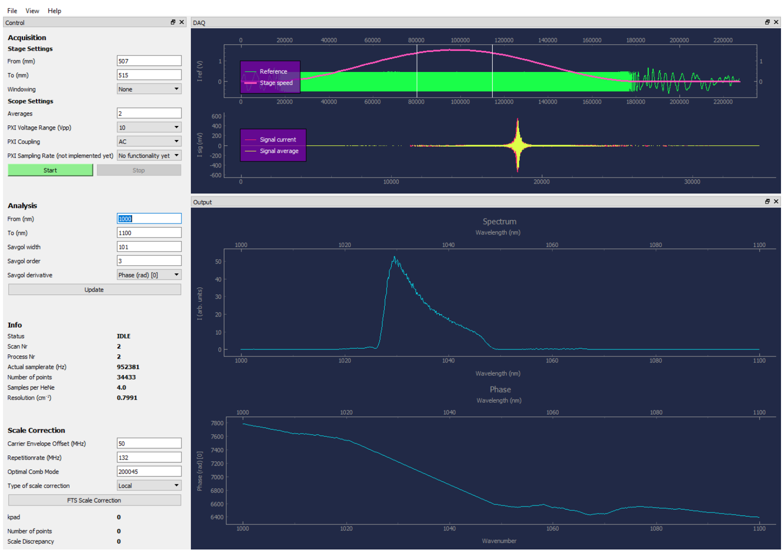

Figure 3.3.: Graphical user interface (GUI) developed for the setup. The code uses only freely available packages based on Python. The GUI is split into two main parts: the control section on the left and the output section on the left. Options for mirror travel range, desired wavelength display range and various other options can be chosen. An information section is constantly updated to provide insight into the ongoing measurement. The last fields on the left are the inputs for the sub-nominal resolution algorithm. The right of the screen is split into two separate windows, a data acquisition (DAQ) and a processing (Output) window. In the former the reference interferogram as well as the mirror speed are shown at the top, with the interferogram of the source to investigate on the bottom. In the output window the spectrum is shown in the upper plot, whereas the phase is shown in the bottom plot.

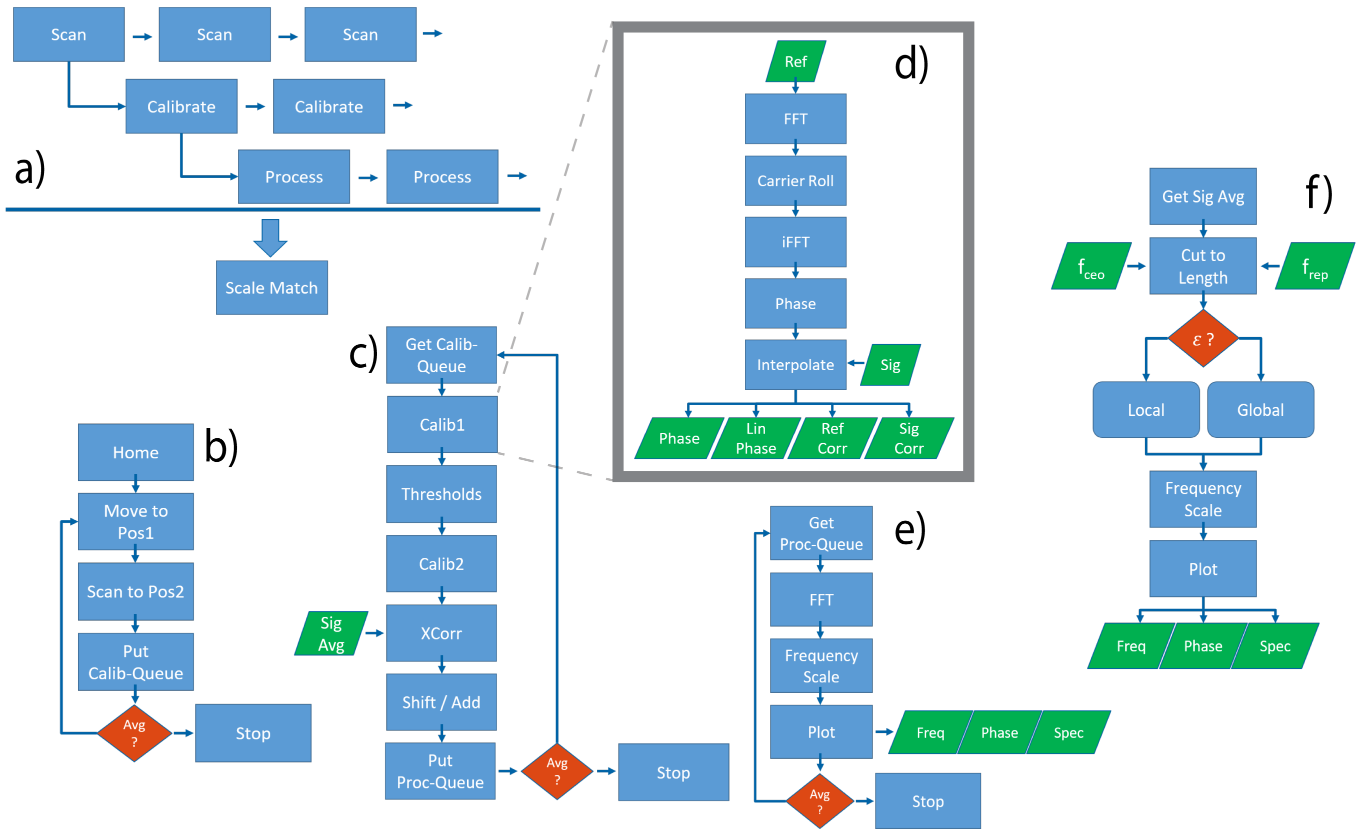

Figure 3.4.: Computation flow charts of the developed code. Processing steps are depicted as blue rectangles and labeled accordingly. Decision knots are illustrated as red diamonds, alternative processes as rectangles with soft edges and data as green parallelograms. The arrows depict the flow of the data through the processes. A basic overview of the multi-threaded system is given in a), the thread coordinating data acquisition is depicted in b). In c) the so-called calibration-thread is shown, which covers the transition from constant time to constant space sampling as well as signal adding. A zoom into this thread is visible in d). The constant space sampled interferograms are queued to the processing-thread shown in e). Finally the flow for sub-nominal resolution is given in f).

3.2.3. Processing Thread

The processing thread is the shortest of the concurrently running threads and visible in figure 3.4 e). An interferogram in the queue is set to AC and Fourier transformed. The phase as well as the spectrum are extracted, while the reference phase is used to determine the frequency index of the reference laser. The ratio of known optical reference frequency and the frequency index gives the spacing of the sampling points in Hz. From this the abscissa of the spectrum can be calculated as frequency, wavenumber or wavelength. The data is forwarded to the graphical user interface, where a fast plotting routine is used to show the acquired reference interferogram with calculated stage speed, the averaged as well as the last recorded signal interferogram, the signal spectrum in an adaptable wavelength interval and the corresponding phase. If the last average is processed, the logic gate stops the processing thread and a signal is triggered, setting the displayed status of the spectrometer from "SCANNING" to "IDLE". Subsequently the measurement can be saved or new measurements can be recorded. If the signal source corresponds to an OFC, an additional thread can be started, enabling the scale-correction thread.

3.2.4. Implementing Sub-nominal Resolution

The general workflow follows the outline given in 2.7 and shown in figure 3.4 f). In a first step, the averaged signal interferogram is trimmed to a length $\Delta_{\max} = c/f_{\text{rep}}$, resulting in a nominal frequency given by f^0_{FTS}. The number of samples per reference laser wavelength is used to calculate the amount of samples to each side of the centerburst, everything outside of this interval is excluded from further processing. It is important to note, that f_{rep} is higher than f^0_{FTS}, and that the symmetric signal is of uneven size, as it contains $2N_0 + 1$ points. Following up, an array matching the OPD of the interferogram is constructed using the knowledge of the interferogram sample spacing

$$\Delta\text{cm} = \frac{1}{N\Delta\tilde{\nu}} \tag{3.2}$$

obtained in the previous section, with size of interferogram N. The centerburst is set to zero retardation and the positions of every other sample point can be calculated using Δcm. The precise information of the retardation of every sample point is crucial for the next steps of the algorithm.

Before code execution, the user specifies whether a local or global scale correction is necessary. We found that usually the former results in kHz levels of mismatch between the frequency scale, for $n - n_{\text{opt}} > 10^3$ with comb mode number of interest n, and mode of perfect overlap n_{opt}. The global correction on the other hand usually delivers kHz levels of mismatch after $n - n_{\text{opt}} > 10^6$, but it is computationally expensive. The local correction follows the description given in 2.7.2, whereas the global correction follows 2.7.3. Attention has to be drawn to the careful reconstruction of the spectrum's abscissa, especially for the global correction, as due to zero-padding the number of points per resolution element increases, with spacing given as natural fraction of f_{rep}. Finally the result is plotted in the user interface and can be stored, delivering a spectrum with sub-nominal resolution.

3.3. Performance Measurements

In order to evaluate the performance of the setup and the associated algorithm, different performance measurements are presented, starting with a time trace of the used NIR source, following with general performance metrics in 3.3.2 consisting of time estimates for measuring and computing the data. In 3.3.3, measurements of the interferogram's modulation efficiency are presented, followed by a set of 100% lines in 3.3.4, giving insight into the time dependent change of the system.

3.3.1. Power Levels of NIR Source

In order to investigate potential power fluctuations of the NIR source used during the measurements, a powermeter (Thorlabs PM100D) was connected with a polarization-maintaining fiber to the NIR source. The power was measured over 24 hours with intervals of two second, starting from August 5^{th} 14:48:28, to August 6^{th} 14:48:28. The measurement together with a rolling average with a window size of 1000 is presented in figure 3.5. Clear modulation is visible, although their scale is limited. A sudden decrease in power is visible after 07:30 a.m., roughly coinciding with the first persons to enter the laboratory that day. For a series of measurements within a 20 minute interval from 06:21 a.m. to 06:41 a.m., the average power was 2.63 ± 0.01 mW. Over the complete measurement duration, the same results were obtained, indicating a stable operation with intrinsic power fluctuations of $\pm$ 0.4%.

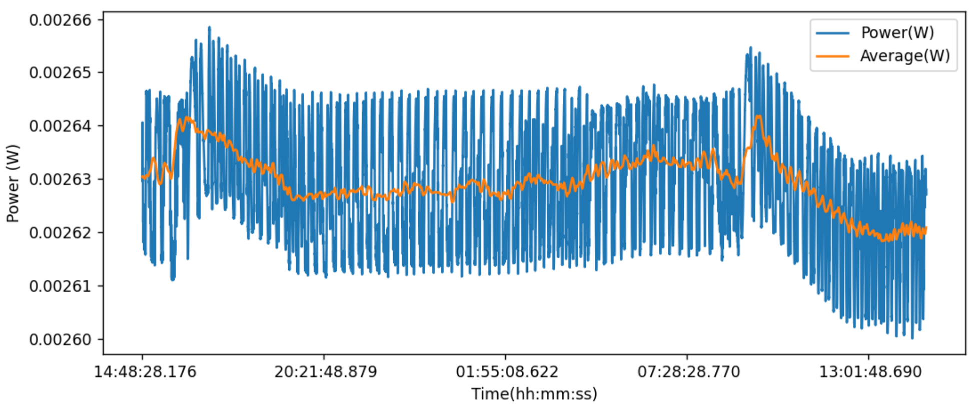

Figure 3.5.: Power level measurements of mode-locked NIR laser used in the FTS setup. The read-out of the powermeter is given in blue as well as a rolling average with a window size of 1000 in order to better visualize the mean value.

3.3.2. Execution Time and General Metrics

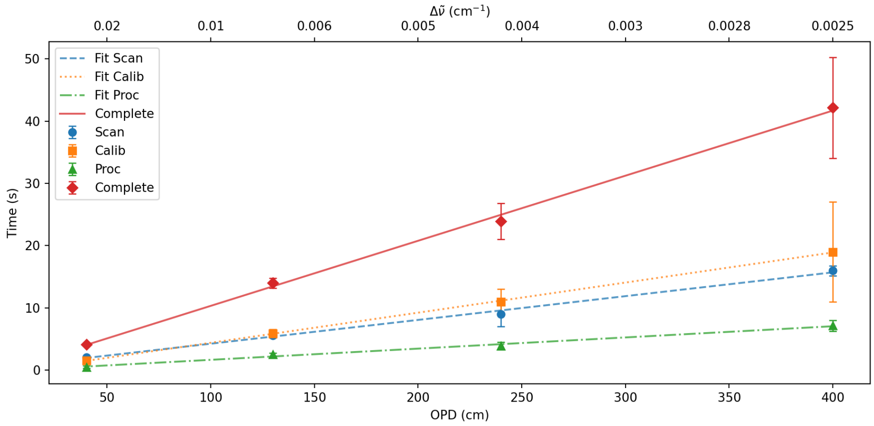

Figure 3.6.: Thread execution time as function of OPD from table 3.1. Blue circles mark the time measurements of the scan thread, orange squares of the calibration thread, green triangles of the processing thread and red diamonds the complete duration for one measurement. The standard deviations are given as error bars. The various lines represent polynomial least squares fits of first order (i.e. $f(x) = kx + d$), with coefficients k, d (0.38, 0.44) for the scan, (0.048, -0.43) for calibration, (0.018, -0.13) for the processing thread and (0.105, -0.117) for the complete measurement.

The successful and economical operation of a spectrometer partially hinges on its duty cycle efficiency. For a spectrometer with sub-nominal resolution, the stability of the OFC plays an additional role. During a single measurement, the comb teeth must not vary by more than half a repetition rate, or else different comb modes will be averaged. The faster the FTS scans, the more leeway can be given to the lock of the OFC. To evaluate the performance of the setup, timestamps were placed in the code to document the execution of the threads described above. Table 3.1 reports the averaged execution times per thread, for four different values of OPD. 400 cm was chosen as it is the maximally achievable retardation, 240 cm because the in-house Ytterbium-based fiber laser runs with a repetition rate of 132 MHz, 130 cm was selected as it would resolve an OFC with repetition rate of 260 MHz. Additionally one tenth of the maximum OPD was chosen to give insight into shorter acquisition times. Five individual measurements per thread are averaged and the standard deviation is given as error estimation.

The measurements are plotted in figure 3.6, with OPD and resolution abscissa. Four polynomial fits of first order are used to fit the data, resulting in the depicted linear functions. The calibration thread overtakes the scan thread at roughly 130 cm and begins to dominate the computation time. Also the standard deviation explodes for longer scans, leading to fluctuating durations for data processing. Note that the time it takes to scan an interferogram varies way less, and thus can be estimated well with the

OPD (cm)	$\Delta\tilde{\nu}$ (cm^{-1})	scan time (s)	calib. time (s)	proc. time (s)	samples
400	0.0025	16.0 ± 0.8	19 ± 8	7.150 ± 0.87	10 529 624
240	0.0042	9 ± 2	11 ± 2	3.9 ± 0.6	5 238 199
130	0.0077	5.6 ± 0.2	5.9 ± 0.7	2.5 ± 0.3	3 397 932
40	0.025	2.09 ± 0.01	1.55 ± 0.03	0.5 ± 0.2	1 006 059

Table 3.1.: Thread execution time measurements for four values of OPD with corresponding resolution and number of samples for four samples per reference laser wavelength $\lambda_{\text{ref}} = 1532.8323$ nm. The mirror speed was chosen as 9 cm/s, in order to keep the sampling frequency below 1 MHz.

travel speed of the mirrors. The complete duration from start of data acquisition to the display of the spectrum increases with 0.1 s per one cm increase in OPD.
While the mirror speed during data acquisition is kept at 9 cm/s, the travel speed during the reversal of the mirror to the starting position is kept at 30 cm/s. The average duty cycle efficiency for a chosen resolution is given in table 3.2. The average over all presented resolutions evaluates to

$$\text{duty cycle efficiency } = 0.84 \pm 0.01 \tag{3.3}$$

indicating that during two consecutive scans, only 16% of the time is spent on moving the mirror to its starting position.

OPD (cm)	duty cycle efficiency
400	0.827 ± 0.007
240	0.82 ± 0.03
130	0.837 ± 0.007
40	0.863 ± 0.001

Table 3.2.: Calculated duty cycle efficiency for different sets of OPD. The mean values and standard deviations of five consecutive measurements are calculated by using the scan time of table 3.1.

3.3.3. Modulation Efficiency

Table 3.3 lists measurements for modulation efficiency of interferograms for different gain settings of the NIR detector PD2 connected in serial to a voltage amplifier (Femto DHPVA-201). The interferograms were recorded over an OPD of 0.8 cm, resulting in quick measurements around ZPD. Due to excess optical power, the beam had to be operated at a lower pump current then usual, in order to stay within the working range of the amplifier as well as the oscilloscope.
For every gain setting, ten DC-interferograms were recorded. The calculated standard deviations from the ten measured interferograms are given as errors on the mean values.

A further increase in gain is unfruitful, as the used amplifier can only produce an output voltage of ± 2 V. The negative values for the minimum voltage are interpreted to be deviations from zero. A set of the measured interferograms is visible in figure 3.7,

Gain(dB)	Imax(mV)	Imin(mV)	DC(mV)	Dark(mV)	$\mathscr{V}$
0	94.21 ± 0.48	-0.64 ± 0.31	46.635 ± 0.058	6.335 ± 0.0018	1.0137 ± 0.0067
10	296.1 ± 1.5	-2.24 ± 0.79	146.20 ± 0.31	11.491 ± 0.0024	1.0152 ± 0.0054
20	903.6 ± 4.2	-38.1 ± 2.8	431.2 ± 1.4	33.9829 ± 0.0078	1.0882 ± 0.0066

Table 3.3.: Modulation efficiency of the NIR interferogram for different gain settings. Imax gives the maximum of the interferogram, Imin gives the minimum value. The DC-level was calculated as mean over all samples, whereas the underlying dark-voltage was measured with a blocked detector. The modulation efficiency, or visibility $\mathscr{V}$ was calculated using equation 2.41.

where the number of samples is plotted against the intensity given in Volt. The complete number of samples amounts to 257894, the location of the centerburst was calculated as the mean of minima and maxima positions to be at sample number

$$\text{ZPD location at } 143090 \pm 72 \tag{3.4}$$

As the resolution of the resulting spectrum was calculated as 1.24 cm^{-1}, the change of OPD between two samples in the interferogram accounts to $\Delta\text{OPD} \approx 3 \cdot 10^{-6}$ cm. From this the deviation of the sampled centerburst to the center of the recorded data can be calculated as

$$\Delta\text{ZPD} = 14143 \text{ samples} \approx 0.042429 \pm 0.2 \cdot 10^{-6} \text{ cm} \tag{3.5}$$

meaning that the interferogram was not recorded perfectly symmetrical.

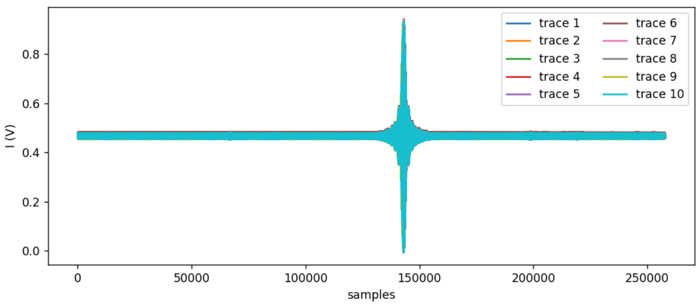

Figure 3.7.: DC measurements of ten interferograms with OPD of 0.8cm and gain of 20dB. Every trace was averaged with two consecutive interferograms.

3.3.4. Photometric precision and 100% lines

100% lines give insight into the change of the system over time and can indicate misalignment, vignetting or variations in the source used. In figure 3.8 eight spectra of the NIR source with resolution of 1.24 cm^{-1} are presented. The spectral overlay in the upper plot shows how good the spectra match each other, a fact that is emphasized with the performance of the 100% line in the bottom plot. The line does not exceed ±5% between 1030 nm and 1045 nm. Notice the poorer performance of trace number six when compared to the others at shorter wavelengths. This is also shown in figure 3.9 , where a clear cave-in is visible for trace number six with regard to calculated SNR. Overall an average SNR of 226 ± 46 was achieved for this set of measurements.

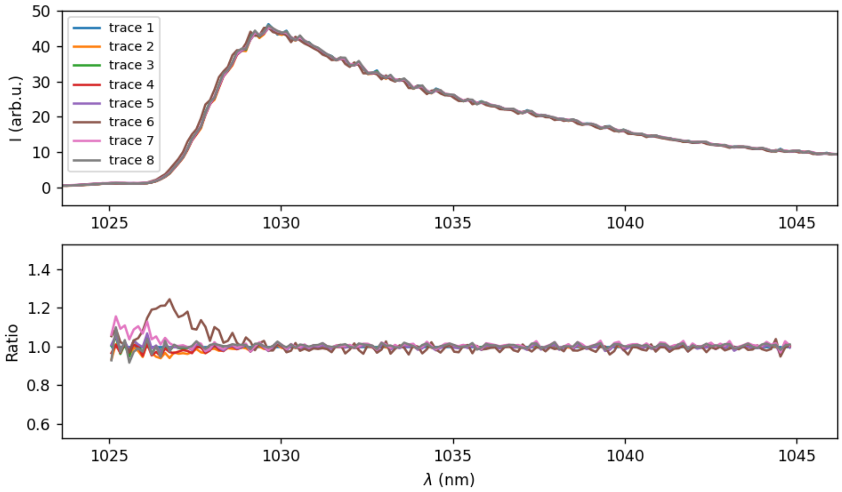

Figure 3.8.: Spectra recorded with 1.24 cm^{-1} resolution on August 28th. Low resolution spectra usually appear smoother than high resolution spectra, as less noise is recorded over the scan. The deviations of the 100% line between 1025 nm and 1030 nm are due to the lack of signal in the region. While the spectrum is plotted over the entire wavelength range, the ratio is only calculated between 1030 nm and 1040 nm. The more the recorded traces deviate from one another, the more the 100% line changes.

Figures 3.10 and 3.11 show the difference between 100% lines for a well aligned source and a badly aligned source. In this case the misalignment was an effect of an instrument rebuild. In figure 3.10 the ratio between the traces remains comparatively flat with only small oscillations around the 100% mark. Whereas the spectra deviate visibly in figure 3.11, they also exhibit more noise leading to higher magnitude of oscillation, while also showing amplified non-linearities between them.

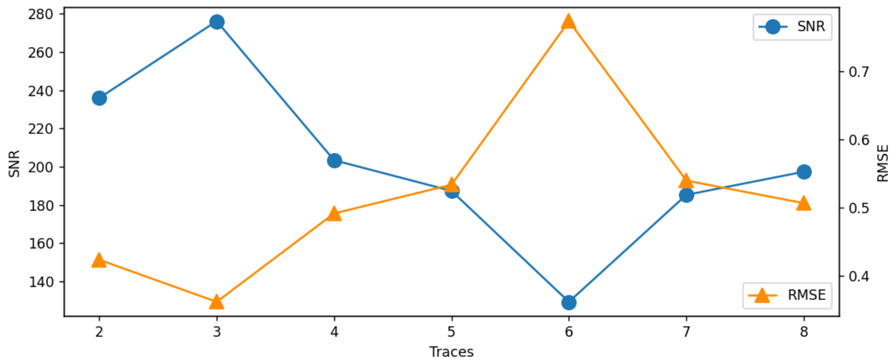

Figure 3.9.: Signal-to-noise ratio and root mean square error of the 100% lines presented in figure 3.8 with respect to the first recorded trace. Blue circles show the SNR (left ordinate axis), orange triangles show the RMSE (right ordinate axis).

3.4. ILS-free spectrum of an OFC

As mentioned at the beginning of 3, we were kindly provided with a set of 10 OFC interferograms from the Nicolaus Copernicus University in Toruń, in order to test our ILS-correction algorithm. The repetition rate of the laser was tuned to 251 MHz and coupled into a cavity with a free spectral range of 250 MHz. The resulting Vernier filtering ratio of 250 resulted in a spectrum of well resolved and spaced comb modes. The reference laser used was a HeNe continuous-wave laser with wavelength of 632.98 nm, whereas the mean values for stabilized f_{ceo} and f_{rep} were calculated from the provided data for every interferogram

$$f_{\text{rep}} = (251213023.375 \pm 0.001) \quad \text{Hz} \tag{3.6}$$

$$f_{\text{ceo}} = (16699999.7 \pm 0.9) \quad \text{Hz} \tag{3.7}$$

After processing the interferograms with the algorithm established in 3.2, a wavenumber resolution of 0.0075 cm^{-1} was obtained, translating to an OPD of 133.3 cm. In order to cut the interferogram to the the desired length of $\Delta_{\text{max}} = \frac{c}{f_{\text{rep}}} \approx 119$ cm, equation 2.53 was used to calculate the necessary number of points to each side of ZPD as $N_0 = 1885306$. The excess samples are thrown away and the thus obtained nominal resolution

$$f^0_{\text{FTS}} = \left(251213019.737954 \pm 10^{-6}\right) \quad \text{Hz} \tag{3.8}$$

of the spectrum evaluates to a relative discrepancy of

$$\varepsilon_0 = (-1.449 \pm 0.004) \cdot 10^{-8} \tag{3.9}$$

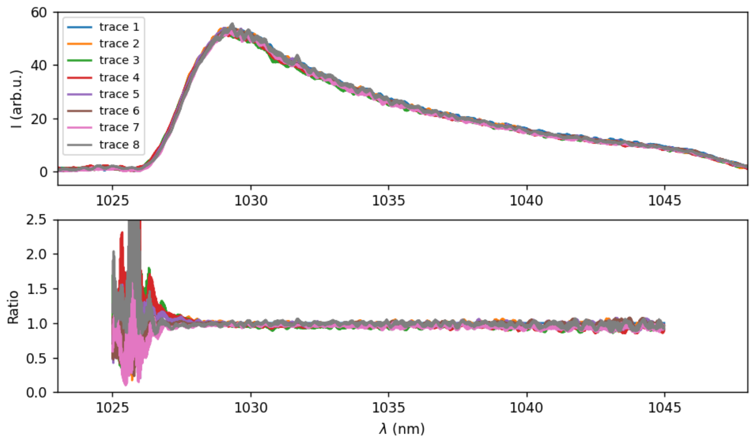

Figure 3.10.: Top: Spectra with good performance of the 100% lines recorded on May 18th, with resolution of 0.026 cm^{-1}. Bottom: 100% lines with respect to the first trace.

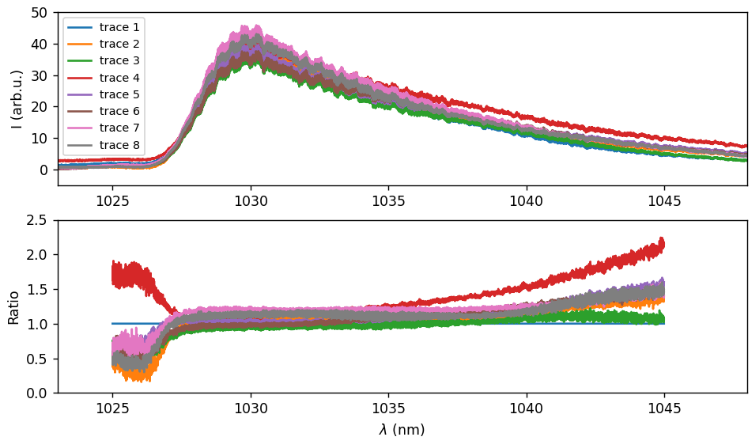

Figure 3.11.: Top: Spectra with poor performance recorded on August 25th, with resolution of 0.026 cm^{-1}. Bottom: 100% lines with respect to the first trace.

using equation 2.54 and standard propagation of uncertainty.

Using the shift procedure as outlined in 2.7.2, the discrepancy between the frequency scale of the FTS and the OFC scale was reduced to zero for a chosen comb mode $n_{\text{opt}} = 756984$. The error between the scales increases with comb modes which are further from this optimal mode following $|n - n_{\mathrm{opt}}|\,\varepsilon_0 f_{\mathrm{rep}}$. This means that a kHz difference is present for n that lie a thousand modes next to n_{opt}. Assuming a broadband spectrum is required with a scale error smaller than this value, an interleaved spectrum for different values of n_{opt} can be produced. The execution time for one optimal comb mode and all the necessary calculations took 1.06 s ± 17.5 ms, which was calculated over seven runs. A part of the local ILS-free spectrum is visible in figure 3.14, increasing magnification on the center mode from a) to c). The comb mode which was chosen for optimization lies 52 wavenumbers away from the mode shown in c), at roughly 6338 cm^{-1}. In a) the effect of the Vernier filtering is visible, with clearly separated comb modes. Below in b), the center three modes are shown, whereas in c) the center mode is depicted. The asymmetric form indicates residual ILS.

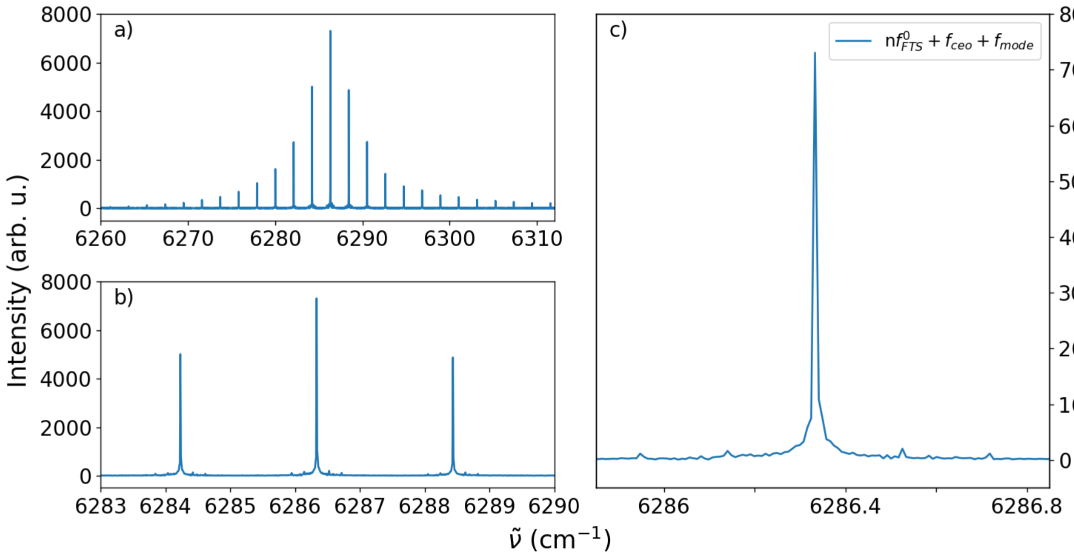

Figure 3.12.: Spectrum of locally ILS-free OFC with Vernier filtering ratio of 250. a) Overview of the region from 6260 to 6310 wavenumbers, b) center three comb modes, c) center mode.

Next the correction for large intervals of comb modes was tested, where the number of zeros $N = 137627336$ padded to both sides of the interferogram was calculated using equation 2.57. In order to find the value of N that reduces the discrepancy the most, a set of integer k_{pad} ranging from zero to 100 were used to find the resulting frequency f_{FTS} for which ε shows its minimum. The different values of the discrepancy are visualized in figure 3.13, where the global minimum in the calculated range is found at $k_{\mathrm{pad}} = 72$. The smaller the initial discrepancy, the higher k_{pad} needs to be, in order to meaningfully reduce ε, as indicated by the local minimum at $k_{\mathrm{pad}} = 36$. The resulting new frequency spacing between the comb modes becomes

$$f_{\mathrm{FTS}} = (251213023.3875806 \pm 0.0000002) \quad \mathrm{Hz} \tag{3.10}$$

meaning that the discrepancy between the frequency scales evaluates to

$$\varepsilon = (5.6 \pm 0.4) \cdot 10^{-11} \tag{3.11}$$

One complete run of the global correction algorithm took 64s $\pm$ 506 ms, averaged over seven runs. It has to be noted, that the process of zero-padding the interferogram also adds additional points to the spectrum, which resolve the ILS. A part of the global ILS-free spectrum is visible in figure 3.14, increasing magnification on the center mode from a) to c), similar to figure 3.12. Comparing the line shown in c) with the one shown for the local correction algorithm, an improvement can be determined in terms of symmetry and linewidth. Side lobes are visible for both procedures, seemingly spaced by equidistant wavenumbers.

With the resulting discrepancy, the computation time can be estimated, which is needed in order to keep the error on the frequency scale at roughly 1 Hz. Assuming the feature of interest in the spectrum is spaced in a 100 nm wide area around 3μm. The corresponding frequency bandwidth evaluates to roughly 3.3 THz, which fit 13271 comb modes for $f_{\mathrm{rep}} = 251$ MHz. The mismatch between the OFC and FTS scales increases with $|n - n_{\mathrm{opt}}|\varepsilon f_{\mathrm{rep}}$. An error of 1 Hz thus appears at

$$|n - n_{\mathrm{opt}}| < 71 \tag{3.12}$$

with discrepancy $\varepsilon = (5.6 \pm 0.4) \cdot 10^{-11}$. For 6635.5 modes to each side of the center, the global sub-nominal resolution algorithm has to be calculated and interleaved 94 times. Excluding the process of interleaving the spectra and neglecting any errors from f_{rep} and ε, the computation time should evaluate to 5981 ± 47s, or roughly 83 minutes.

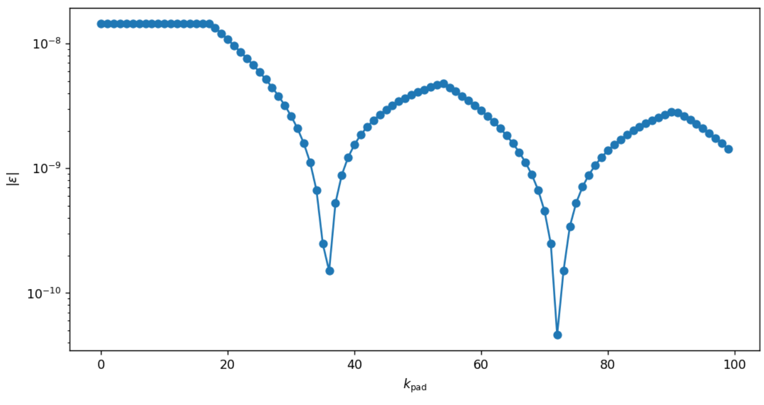

Figure 3.13.: Relative discrepancy between the OFC and the FTS scale for different values of k_{pad}. The global minimum of this plot is located at $k_{\mathrm{pad}} = 72$. The smaller the initial discrepancy ε_0 after the truncation and shit procedures, the higher the value for k_{pad} has to be, to meaningfully reduce $|\varepsilon|$.

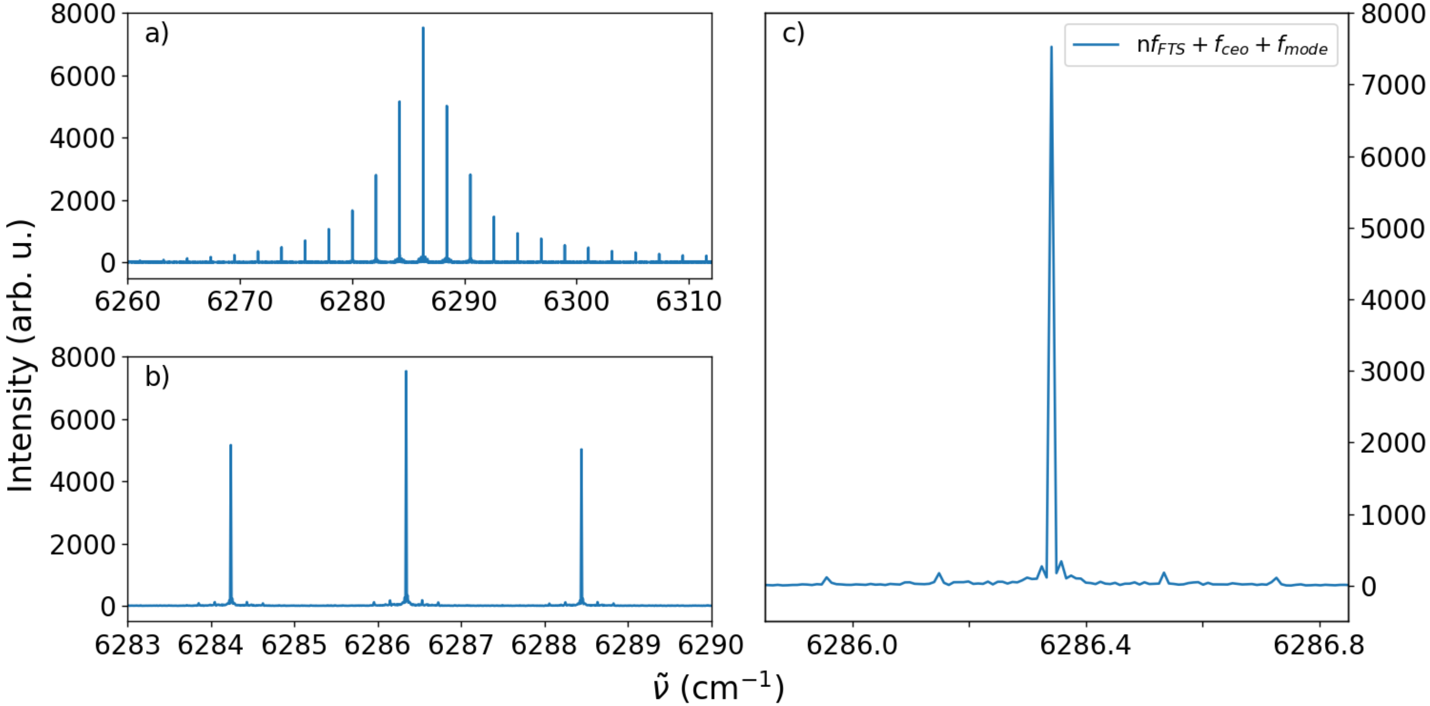

Figure 3.14.: Globally ILS-free OFC spectrum with Vernier filtering ratio of 250. Only every $(k_{\text{pad}} + 2)$-th point is plotted, excluding the resolved ILS. a) Overview of the region from 6260 to 6310 wavenumbers, due to the Vernier filtering ratio the visible comb modes are easily resolved. b) Center three comb modes from 6238 to 6290 wavenumbers c) Center mode corresponding to $n = 750199$ with distinctive side lobes at equal distances.

4. Discussion and Conclusion

The spectrometer setup meets the requirements outlined in 1.2 and furthermore demonstrates a duty cycle efficiency of 0.84 ± 0.01, which is on par with commercial devices [19, pp. 51, 107]. The freely choosable resolution up to 0.0025 cm^{-1} lets the user pick the optimal settings for their application, which is in contrast to other devices like the Thorlabs Redstone OSA305, which only offers three preset resolutions [21]. The software execution time, as shown in figure 3.6 and table 3.1, shows promising individual results. Especially the low scan time together with the high duty cycle efficiency indicate, that the setup can comfortably record OFC-interferograms, even if they can only be stabilized for a small amount of minutes. For example, an OFC with repetition rate of 260 MHz, recorded with OPD of 130 cm, stable during 10 minutes of data acquisition, will be recorded 107 times.

Power fluctuations of the used mode-locked laser are on the order of $\pm$ 0.4 %, which, compared to table 3.3, explain the value of the standard deviation for the measured maximum intensity (Imax). The measured modulation efficiency shows strong results, approaching the ideal of 100% modulation depth for all tested gain settings. The precise location of the point of ZPD helps to record more symmetric interferograms in the future, leading to less phase nonlinearities and reduced leakage. The photometric precision of the instrument suffers from slight misalignment with regards to the two interferometer arms as shown in 3.3.4, as expected from theory (see 2.1). Thus it is vital to align the interferometer as precisely as possible prior to measurements. As the 1532.8 nm reference laser is invisible to the eye, adding a NIR beam profiler will allow for improved instrument alignment. Remaining etalons due to planar detector windows are an additional concern that needs to be addressed in the future. As the setup was designed for application in the MIR, the employed NIR detectors feature flat windows, which explain remaining etalon features in the recorded signals.

Concerning the effort of implementing the algorithm outlined in [12], [13] in Python, we demonstrated proper functionality by benchmarks as well as comparison to previous evaluations with another routine. Our algorithm was capable of matching the sample spacing of the FTS to the repetition rate of the provided OFC up to a relative discrepancy of $\varepsilon = (5.6 \pm 0.4) \cdot 10^{-11}$, demonstrating the capability of achieving linewidth-limited resolution. Our results are in agreement with the evaluation provided by our collaborators in Poland for the same data, with differences on the level of machine precision. Open questions still remain with regard to the sidelobes visible after ILS correction, as seen in figure 3.14 c). However, these are present in our evaluation as well as our collaborator's results. Likely explanations include shortcomings in the experimental setup, and remaining distortion by the ILS, introduced by the residual mismatch between the sampling and OFC scales.

In summary, we demonstrated the successful implementation of the algorithm to obtain ILS-free spectra. This included the proof-of-principle demonstration of sub-nominal resolution with data obtained from a cavity-filtered OFC. Next steps would be to continue to work on the system, keeping the experimental operation stable, frequently measuring 100% lines and optimizing the algorithm where possible.
A different change in the setup will be the switch to a sub-Hz stable reference laser within in the following year. Since the accuracy of the reference laser is critical for the relative discrepancy ε (see 2.7.4, this highly stable reference should deliver accuracy η of magnitude 10^{-15} for wavelength of 1550 nm and 1 Hz of linewidth. Assuming a SNR of 250 and $n_{\mathrm{abs}} = 750000$ (equivalent to $\approx 3\mu$m), the required stability limit of the reference would be $\eta_{\mathrm{lim}} = 4 \cdot 10^{-9}$, following equation 2.63. The currently employed reference laser does not meet this stability and needs to be replaced to enable the full potential of the instrument.

Regarding the goal of precision spectroscopy, further updates include baseline correction, spectral line fitting and statistical evaluation tools. Additionally the process of interleaving spectra with sub-nominal resolution will require a well-optimized algorithm, minimizing the computation time as much as possible. Especially interesting is the possibility of combining the sub-nominal resolution spectra with dimensionality reduction techniques like Principal Component Analysis [55], together with learning algorithms for classification. This could result in completely automated spectral retrieval with the possibility to process and classify a multitude of spectral features.

List of Figures

List of Tables

Bibliography

[1] G. S. Nikolic, M. D. Cakic, and D. J. Cvetkovic, *Fourier Transforms*. Rijeka: IntechOpen, Feb 2017.

[2] P. L. Hanst, "Air pollution measurement by Fourier transform spectroscopy," *Applied Optics*, vol. 17, no. 9, pp. 1360–1366, 1978.

[3] H. Kuzmany, *Solid-State Spectroscopy : An Introduction*. Heidelberg [u.a.]: Springer, 2. ed.. ed., 2009.

[4] L. W. Perner, G. Winkler, G.-W. Truong, D. Follman, J. Fellinger, M. Prinz, S. Puchegger, G. D. Cole, and O. H. Heckl, "High-accuracy measurement of mid-ir refractive indices of gaas/algaas in thin-film multilayers," in *Optical Interference Coatings Conference (OIC) 2022*, p. WA.5, Optica Publishing Group, 2022.

[5] P. Jakobsen, P. Ferruit, C. Alves de Oliveira, *et al.*, "The Near-Infrared Spectrograph (NIRSpec) on the James Webb Space Telescope: I. Overview of the instrument and its capabilities," *Astronomy & Astrophysics*, vol. 661, p. A80, 2022.

[6] G. H. Rieke, G. S. Wright, T. Böker, *et al.*, "The Mid-Infrared Instrument for the *James Webb Space Telescope*, I: Introduction," *Publications of the Astronomical Society of the Pacific*, vol. 127, pp. 584–594, jul 2015.

[7] I. Gordon, L. Rothman, R. Hargreaves, *et al.*, "The HITRAN2020 molecular spectroscopic database," *Journal of quantitative spectroscopy & radiative transfer*, vol. 277, p. 107949, 2022.

[8] J. Mandon, G. Guelachvili, N. Picqué, F. Druon, and P. Georges, "Femtosecond laser Fourier transform absorption spectroscopy," *Optics letters*, vol. 32, no. 12, pp. 1677–1679, 2007.

[9] E. Sorokin, I. Sorokina, J. Mandon, G. Guelachvili, and N. Picqué, "Sensitive multiplex spectroscopy in the molecular fingerprint 2.4 µm region with a Cr2+:ZnSe femtosecond laser," *Optics express*, vol. 15, no. 25, pp. 16540–16545, 2007.

[10] N. Picqué, J. Mandon, and G. Guelachvili, "Fourier transform spectroscopy with a laser frequency comb," *Nature photonics*, vol. 3, no. 2, pp. 99–102, 2009.

[11] N. Picque and T. W. Haensch, "Frequency comb spectroscopy," *Nature photonics*, vol. 13, no. 3, pp. 146–157, 2019.

[12] P. Maslowski, K. F. Lee, A. C. Johansson, A. Khodabakhsh, G. Kowzan, L. Rutkowski, A. A. Mills, C. Mohr, J. Jiang, M. E. Fermann, and A. Foltynowicz, "Surpassing the path-limited resolution of Fourier-transform spectrometry with frequency combs," *Physical Review A*, vol. 93, no. 2, p. 021802(R), 2016.

[13] L. Rutkowski, P. Masłowski, A. C. Johansson, A. Khodabakhsh, and A. Foltynowicz, "Optical frequency comb Fourier transform spectroscopy with sub-nominal resolution and precision beyond the Voigt profile," *Journal of Quantitative Spectroscopy and Radiative Transfer*, vol. 204, pp. 63–73, 2018.

[14] A. Hjältén, M. Germann, K. Krzempek, A. Hudzikowski, A. Głuszek, D. Tomaszewska, G. Soboń, and A. Foltynowicz, "Optical frequency comb Fourier transform spectroscopy of 14N216O at 7.8 μm," *Journal of Quantitative Spectroscopy and Radiative Transfer*, vol. 271, p. 107734, 2021.

[15] D. Charczun, G. Kowzan, A. Cygan, R. S. Trawiński, D. Lisak, and P. Masłowski, "Broadband and high resolution measurements of cavity loss and dispersion," *Photonics letters of Poland*, vol. 10, no. 2, pp. 48–50, 2018.

[16] G. Winkler, L. Perner, G.-W. Truong, G. Zhao, D. Bachmann, A. Mayer, J. Fellinger, D. Follman, P. Heu, C. Deutsch, D. Bailey, H. Peelaers, S. Puchegger, A. Fleisher, G. Cole, and O. Heckl, "Mid-infrared interference coatings with excess optical loss below 10 ppm," *Optica*, vol. 8, no. 5, pp. 686–696, 2021.

[17] A. A. Michelson and E. W. Morley, "On the relative motion of the Earth and the luminiferous ether," *American journal of science (1880)*, vol. s3-34, no. 203, pp. 333–345, 1887.

[18] J. B. Bates, "Fourier Transform Infrared Spectroscopy," *Science*, vol. 191, no. 4222, pp. 31–37, 1976.

[19] P. R. Griffiths, *Fourier transform infrared spectrometry*. Chemical analysis ; ; v. 171, Hoboken, N.J. :: Wiley-Interscience,, 2nd ed.. ed., 2007.

[20] S. P. Davis, *Fourier transform spectrometry*. San Diego :: Academic Press,, 2001.

[21] Thorlabs, "Redstone OSA305." `[Accessed:2022-08-30]{https://www.thorlabs.com/newgrouppage9.cfm?objectgroup_id=5276&pn=OSA305}`.

[22] Bruker, "VERTEX 80/80v FT-IR Spectrometers." `[Accessed:2022-08-30]{https://www.bruker.com/en/products-and-solutions/infrared-and-raman/ft-ir-research-spectrometers/vertex-research-ft-ir-spectrometer/vertex-80-80v-ft-ir-spectrometer.html}`.

[23] Bruker, "IFS 125HRs." `[Accessed:2022-08-30]{https://www.bruker.com/en/products-and-solutions/infrared-and-raman/ft-ir-research-spectrometers/ifs-125hr-high-resolution-ft-ir-spectrometer.html}`.

[24] J. W. Brault, “New approach to high-precision Fourier transform spectrometer design,” *Applied Optics*, vol. 35, no. 16, pp. 2891–2896, 1996.

[25] M. V. R. K. Murty, “Modification of Michelson Interferometer Using Only One Cube-Corner Prism,” *Journal of the Optical Society of America (1930)*, vol. 50, no. 1, p. 83, 1960.

[26] B. E. A. Saleh, *Optik und Photonik.* Weinheim: Wiley-VCH, dritte, vollständig überarbeitete und erweiterte auflage. ed., 2020.

[27] T. H. MAIMAN, “Stimulated Optical Radiation in Ruby,” *Nature (London)*, vol. 187, no. 4736, pp. 493–494, 1960.

[28] R. Paschotta, “Pulse Generation.” `[Accessed:2022-08-30]{https://www.rp-photonics.com/pulse_generation.html}`.

[29] R. Paschotta, “Mode Locking.” `[Accessed:2022-08-30]{https://www.rp-photonics.com/mode_locking.html}`.

[30] U. Keller, “Recent developments in compact ultrafast lasers,” *Nature (London)*, vol. 424, no. 6950, pp. 831–838, 2003.

[31] J. Wahlstrand, J. Willits, C. Menyuk, and S. Cundiff, “The quantum-limited comb lineshape of a mode-locked laser: Fundamental limits on frequency uncertainty,” *Optics express*, vol. 16, no. 23, pp. 18624–18630, 2008.

[32] M. Endo, T. D. Shoji, and T. R. Schibli, “Ultralow Noise Optical Frequency Combs,” *IEEE journal of selected topics in quantum electronics*, vol. 24, no. 5, pp. 1–13, 2018.

[33] D. J. Jones, S. A. Diddams, J. K. Ranka, A. Stentz, R. S. Windeler, J. L. Hall, and S. T. Cundiff, “Carrier-Envelope Phase Control of Femtosecond Mode-Locked Lasers and Direct Optical Frequency Synthesis,” *Science (American Association for the Advancement of Science)*, vol. 288, no. 5466, pp. 635–639, 2000.

[34] H. Telle, G. Steinmeyer, A. Dunlop, J. Stenger, D. Sutter, and U. Keller, “Carrier-envelope offset phase control: A novel concept for absolute optical frequency measurement and ultrashort pulse generation,” *Applied physics. B, Lasers and optics*, vol. 69, no. 4, pp. 327–332, 1999.

[35] K. Holman, R. Jones, A. Marian, S. Cundiff, and J. Ye, “Detailed studies and control of intensity-related dynamics of femtosecond frequency combs from mode-locked Ti:sapphire lasers,” *IEEE journal of selected topics in quantum electronics*, vol. 9, no. 4, pp. 1018–1024, 2003.

[36] F. Helbing, G. Steinmeyer, and U. Keller, “Carrier-envelope offset phase-locking with attosecond timing jitter,” *IEEE journal of selected topics in quantum electronics*, vol. 9, no. 4, pp. 1030–1040, 2003.

[37] N. R. Newbury and W. C. Swann, "Low-noise fiber-laser frequency combs (Invited)," *Journal of the Optical Society of America. B, Optical physics*, vol. 24, no. 8, pp. 1756–1770, 2007.

[38] D. Walker, T. Udem, C. Gohle, B. Stein, and T. Iianscii, "Frequency dependence of the fixed point in a fluctuating frequency comb," *Applied physics. B, Lasers and optics*, vol. 89, no. 4, pp. 535–538, 2007.

[39] A. Apolonski, A. Poppe, G. Tempea, C. Spielmann, T. Udem, R. Holzwarth, T. Hänsch, and F. Krausz, "Controlling the phase evolution of few-cycle light pulses," *Physical review letters*, vol. 85, no. 4, pp. 740–743, 2000.

[40] A. S. Zachor and S. M. Aaronson, "Delay compensation: Its effect in reducing sampling errors in fourier spectroscopy," *Applied Optics*, vol. 18, no. 1, pp. 68–75, 1979.

[41] ASTM, "ASTM E 1944-98 (Reapproved 2002): Standard Practice for Describing and Measuring Performance of Laboratory Fourier Transform Near-Infrared (FT-NIR) Spectrometers: Level Zero and Level One Tests," standard, American Society for Testing and Materials, 100 Barr Harbor Drive, PO Box C700, West Conshohocken, PA 19428-2959, United States, 1998.

[42] B. A. Shenoi, *Introduction to Digital Signal Processing and Filter Design.* Chichester: Wiley-Interscience, 1. aufl. ed., 2005.

[43] D. Stranneby, *Digital signal processing : DSP and applications /.* Oxford ; Boston :: Newnes,, 2001.

[44] S. V. Vaseghi, *Advanced Digital Signal Processing and Noise Reduction.* Hoboken: Wiley, 4. aufl. ed., 2008.

[45] H. Nyquist, "Certain Topics in Telegraph Transmission Theory," *Transactions of the American Institute of Electrical Engineers*, vol. 47, no. 2, pp. 617–644, 1928.

[46] E. O. Brigham, *The fast fourier transform.* Englewood Cliffs, NJ: Prentice-Hall, 1974.

[47] G. Brooker, *Modern classical optics.* Oxford master series in physics ; Atomic, optical, and laser physics ; ; 8, Oxford ; New York :: Oxford University Press,, 2003.

[48] L. Mertz, *Transformations in optics.* New York, NY [u.a.]: Wiley, 1965.

[49] M. L. Forman, W. H. Steel, and G. A. Vanasse, "Correction of Asymmetric Interferograms Obtained in Fourier Spectroscopy∗," *J. Opt. Soc. Am.*, vol. 56, pp. 59–63, Jan 1966.

[50] Aerotech, "ACT115DL Direct-Drive Linear Actuator." `[Accessed: 2022-09-06]{https://www.aerotech.com/product/stages-actuators/act115dl-direct-drive-linear-actuator/}`.

[51] G. Kowzan, D. Charczun, A. Cygan, R. S. Trawiński, D. Lisak, and P. Masłowski, "Broadband Optical Cavity Mode Measurements at Hz-Level Precision With a Comb-Based VIPA Spectrometer," *Scientific reports*, vol. 9, no. 1, pp. 8206–8206, 2019.

[52] D. Lisak, D. Charczun, A. Nishiyama, T. Voumard, T. Wildi, G. Kowzan, V. Brasch, T. Herr, A. J. Fleisher, J. T. Hodges, R. Ciuryło, A. Cygan, and P. Masłowski, "Dual-comb cavity ring-down spectroscopy," *Scientific reports*, vol. 12, no. 1, pp. 2377–2377, 2022.

[53] Thorlabs, "Quantum Cascade Lasers: Fabry-Perot, Two-Tab C-Mount." `[Accessed:2022-08-30]{https://www.thorlabs.com/newgrouppage9.cfm?objectgroup_id=6826&pn=QF4550CM1}`.

[54] M. Takeda, H. Ina, and S. Kobayashi, "Fourier-transform method of fringe-pattern analysis for computer-based topography and interferometry," *Journal of the Optical Society of America (1930)*, vol. 72, no. 1, pp. 156–160, 1982.

[55] K. Pearson, "LIII. On lines and planes of closest fit to systems of points in space," *The London, Edinburgh and Dublin philosophical magazine and journal of science*, vol. 2, no. 11, pp. 559–572, 1901.

A. Appendix

James Webb Space Telescope	JWST
Fourier transform spectrometer	FTS
Optical frequency comb	OFC
Fourier transform infrared	FTIR
Optical path difference	OPD
Zero path difference	ZPD
Fourier transform	FT
Instrumental line shape	ILS
Full width at half maximum	FWHM
Continuous-Wave	cw
White-light-source	WLS
Signal-to-noise ratio	SNR
Digital signal processing	DSP
Analog to digital converter	ADC
Sigma-delta	$\Sigma\Delta$
Fast Fourier transform	FFT
Discrete complex Fourier transform	DFT
Position 1	Pos1
Position 2	Pos2
Graphical user interface	GUI
Data Acquisition	DAQ
Near-infrared	NIR
Mid-infrared	MIR

Table A.1.: Abbreviations

Linear stage	Aerotech	ACT115DL
Reference laser	Thorlabs	Redstone OSA305
NIR-collimation package	Thorlabs	F260APC-1064 an
MIR-collimation package	Thorlabs	F028FC-4950
Reference-collimation package	Thorlabs	F260APC-1550
Gold mirrors 1"	Thorlabs	PF10-03-M02
Gold mirrors 2"	Thorlabs	PF20-03-M02
Non-polarizing beamsplitter	Thorlabs	BSW521
Retroreflectors	Edmund Optics	49674
D-shaped gold mirrors	Thorlabs	PFD10-03-M02
MIR-lenses for detector	Thorlabs	LA5315-E
MIR detector	Vigo	NIPM-I-5
Silver mirror 1"	Thorlabs	PF10-03-P01
NIR-lens for reference detector	Thorlabs	LA1074-C-ML
Reference-detector	Thorlabs	PDAPC4
NIR-lens for NIR detector	Thorlabs	LA1074-C-ML
NIR-detector	Thorlabs	PDAPC4
Oscilloscope	National Instruments	PXI-5922

Table A.2.: Setup Components

Powermeter	Thorlabs	PM100D
Optical Spectrum Analyzer	Thorlabs	Redstone OSA305
MIR quantum cascade laser	Thorlabs	QF4550CM1
Collimated laser diode module 635 nm	Thorlabs	CPS635R

Table A.3.: Additional Instruments